

A Homogeneous Catalog of Oscillating Solar-Type Stars Observed by the Kepler Mission and a New Amplitude Scaling Relation Including Chromospheric Activity

MARYUM SAYEED ¹, DANIEL HUBER ^{2,3}, ASHLEY CHONTOS ⁴, AND YAGUANG LI ²

¹*Department of Astronomy, Columbia University, 550 West 120th Street, New York, NY 10027, USA*

²*Institute for Astronomy, University of Hawai‘i, 2680 Woodlawn Drive, Honolulu, HI 96822, USA*

³*Sydney Institute for Astronomy (SfA), School of Physics, University of Sydney, NSW 2006, Australia*

⁴*Department of Astrophysical Sciences, Princeton University, 4 Ivy Lane, Princeton, NJ 08544, USA*

ABSTRACT

We present a homogeneous catalog of global asteroseismic parameters and derived stellar parameters for 765 *Kepler* main-sequence and subgiant stars. The catalog was produced by re-analyzing all available *Kepler* DR25 short-cadence data using pySYD, an automated pipeline to extract global asteroseismic parameters. We find 50 new detections, seven of which are also planet candidate host stars. We find excellent agreement between our ν_{\max} and $\Delta\nu$ measurements and literature values, with an average offset of $0.2 \pm 0.4\%$ ($\sigma = 5\%$) and $0.2 \pm 0.7\%$ ($\sigma = 2\%$), respectively. In addition, we derive stellar radii and masses with an average precision of 2.7% and 10.4%, respectively, and find a mean offset of $0.8 \pm 0.2\%$ ($\sigma = 6\%$) between our radii derived with asteroseismology and those from *Gaia* parallaxes. Using spectroscopic $\log R'_{\text{HK}}$ activity measurements from Keck/HIRES, we derive an amplitude scaling relation with an activity term for main-sequence and subgiant stars, which successfully predicts amplitudes with a precision of $\approx 8\text{--}9\%$. Our work is the largest and most homogeneous asteroseismic catalog of *Kepler* main-sequence and subgiant stars to date, including a total of 101 stars hosting planet candidates and 451 stars with measured rotation periods.

Keywords: Asteroseismology (73) – fundamental parameters (555) – stellar oscillations (1617) – photometry (1234)

1. INTRODUCTION

Asteroseismology, the study of stellar oscillations, is a powerful method for constraining fundamental stellar properties. Advances in photometric time-series observations from space-based missions like CoRoT (Baglin et al. 2006), *Kepler* (Borucki et al. 2010; Koch et al. 2010) and NASA’s Transiting Exoplanet Survey Satellite (TESS, Ricker et al. 2014) have revolutionized asteroseismology for stars across the Hertzsprung–Russell (H–R) diagram. This technique provides valuable insight into stellar interiors including classification of evolutionary stages (e.g. Bedding et al. 2011), measurement of internal rotation (e.g., Beck et al. 2012), and detection of magnetic fields (e.g., Fuller et al. 2015; Cantiello et al. 2016; Stello et al. 2016; Li et al.

2020a). Furthermore, it advances our knowledge of galaxy evolution (e.g., Hon et al. 2021), and enables precise characterization of exoplanet host stars (e.g., Johnson et al. 2010; Huber et al. 2013; Lundkvist et al. 2016).

For solar-like oscillations, the power excess can be characterized through two global asteroseismic parameters: the frequency of maximum power (ν_{\max}) and the average large frequency separation ($\Delta\nu$). Combined with scaling relations, these parameters provide an efficient method to derive fundamental stellar parameters such as mass, radius, surface gravity, and density. More precise stellar properties such as ages can be inferred through modeling individual frequencies (e.g., Metcalfe et al. 2010; Batalha et al. 2011; Howell et al. 2012; Carter et al. 2012; Metcalfe et al. 2012; Silva Aguirre et al. 2013; Gilliland et al. 2013; Chaplin & Miglio 2013; Silva Aguirre et al. 2015, 2017). However, this is often not possible for stars with low signal-to-noise (SNR) or short time-series

with limited frequency resolution. Large, homogeneous catalogs of global asteroseismic parameters therefore remain a fundamental benchmark in stellar astrophysics.

In addition to inferring ages, large catalogs of asteroseismic parameters enable the study of the effect of stellar activity on suppressed solar-like oscillations. Stellar activity and magnetic fields are known to decrease oscillation amplitudes (Chaplin et al. 2000; Komm et al. 2000; García et al. 2010; Mathur et al. 2019), but this effect has neither been quantified nor incorporated in amplitude scaling relations. The mechanism for this amplitude suppression is still unclear, but stellar activity has been suggested as a dominating factor (e.g., Mosser et al. 2009; Dall et al. 2010; Gaulme et al. 2014; Corsaro et al. 2024). For instance, some have studied the effects of binary interactions (Gehan et al. 2022, 2024) and chromospheric activity (e.g., Bonanno et al. 2014) on oscillation amplitudes. Large, homogeneous catalogs of solar-like oscillators which overlap with spectroscopic data are required to advance our understanding of amplitude scaling relations.

NASA’s *Kepler* mission observed $\sim 196,000$ stars in long-cadence (29.4 minutes) mode, which is sufficient to sample oscillations in red giant stars (e.g., Hekker et al. 2011a; Huber et al. 2011; Stello et al. 2013; Huber et al. 2014; Mathur et al. 2016; Yu et al. 2016). Main-sequence and subgiant stars require sampling in short-cadence (58.5 seconds), which was obtained for only ~ 500 pre-selected stars during each observing quarter; fundamental parameters for this sample were provided in Chaplin et al. (2014). Since then, the *Kepler* Science Office released newly calibrated data with improved data processing, such as smear correction and aperture image extension (Thompson et al. 2016). Furthermore, while there have been additional discoveries of seismic detections in main-sequence and subgiant stars (e.g., White et al. 2012; Creevey et al. 2012; Gaulme et al. 2013; Doğan et al. 2013; Li et al. 2020b; Balona 2020; Mathur et al. 2022; Bhalotia et al. 2024), they employ different methods to measure global asteroseismic quantities, which can lead to systematic offsets in derived stellar properties across the H–R diagram.

In this paper, we use a single, well-tested and open-source asteroseismic pipeline (pySYD, Chontos et al. 2022), to extract global asteroseismic parameters and determine stellar properties for main-sequence and subgiant stars observed in *Kepler* re-calibrated short-cadence data. pySYD is adapted from the framework of the IDL-based SYD pipeline, and has been used to extract asteroseismic parameters for many *Kepler* stars

Table 1. Summary of previously known solar-like oscillators re-analyzed with pySYD for this work. Section 2.1 provides reasoning for the difference in the number of stars in a given catalog and those re-analyzed.

Source catalog	Targets		
	Total	Re-analyzed	Confirmed
Serenelli et al. (2017)	415	398	396
Chaplin et al. (2014)	518	111	111
Mathur et al. (2022)	624	97	94
Balona (2020)	70	13	11
Huber et al. (2013)	77	72	70
Lundkvist et al. (2016)	102	38	25
Li et al. (2020a)	36	1	1
Pinsonneault et al. (2018)	6676	1	1
Lund et al. (2017)	66	2	2
Mosser et al. (2014)	1178	1	1
White et al. (2012)	163	1	1
Chontos et al. (2019)	1	1	1
Bhalotia et al. (2024)	1	1	1

(e.g., Huber et al. 2011; Bastien et al. 2013; Chaplin et al. 2014; Serenelli et al. 2017; Yu et al. 2018). We provide a homogeneous catalog of asteroseismic stellar masses, radii, and global oscillation parameters for 765 solar-like oscillators in *Kepler*.

2. OBSERVATIONS AND DATA ANALYSIS

2.1. Target Selection

We started with the full list of *Kepler* stars observed in short-cadence from Mikulski Archive for Space Telescopes (MAST), resulting in a total of 5678 unique stars. We first removed stars with detected oscillations in long-cadence data (Yu et al. 2018) (5391 remaining), eclipsing binaries (Kirk et al. 2016) (4810 remaining), and Delta Scuti pulsators (Murphy et al. 2019) which are too hot to show solar-like oscillations. For the remaining 4346 targets, we flagged stars that were already reported in previous studies to keep track of new detections in our sample. The following is a breakdown of previous asteroseismic detections:

- (i) 415 stars from Serenelli et al. (2017), but one was a binary (Kirk et al. 2016), two were observed in long-cadence (Yu et al. 2018), and 14 are exoplanet hosts; 398 stars remain in which to search for solar-like oscillations.
- (ii) 518 stars from Chaplin et al. (2014), but 407 overlapped with S17; 111 stars remain.

- (iii) 624 stars from Mathur et al. (2022), but 524 were already known detections, and three were found to be binaries; 97 stars remain.
- (iv) 70 stars from Balona (2020), but 56 were already known detections (in Serenelli et al. (2017), Chaplin et al. (2014), or Mathur et al. (2022)), and one was an eclipsing binary; 13 stars remain.
- (v) 117 exoplanet hosts from Huber et al. (2013) and Lundkvist et al. (2016), but three were not observed in short-cadence (KIC 4476423, 8219268, 9088780), and six are binaries (KIC 2306756, 4769799, 5652983, 6678383, 8554498, 8803882); 108 stars remain.

We also performed a systematic search for oscillations in *Kepler* exoplanet hosts. Of the total 3611 stars given an exoplanet disposition of confirmed or candidate on the NASA Exoplanet Archive (NASA Exoplanet Archive 2024), 766 stars were observed in short-cadence, of which eight targets were removed since they are classified as Delta Scuti pulsators or already detections in long-cadence data (Yu et al. 2018). In summary, we re-analyzed *Kepler* DR25 data for 4346 stars, of which 758 were confirmed or candidate exoplanet hosts. Table 1 provides a breakdown of the number of targets analyzed from each source catalog.

2.2. Data Preparation

Before running our analysis, we prepared all light curves using the following steps:

- (i) We downloaded Pre-Search Data Conditioning Simple Aperture Photometry (PDCSAP) from MAST using `lightkurve` (Lightkurve Collaboration et al. 2018) with good quality flags (`SAP_QUALITY=0`). All available *Kepler* quarters were stitched together using the `stitch()` function in `lightkurve`, and used in the subsequent analysis.
- (ii) We performed a sigma-clipping routine, and removed outliers greater than 5σ .
- (iii) We applied a smoothing Savitzky-Golay filter of 1-day to remove any long-periodic (low-frequency) variations, and normalized the resulting flux.
- (iv) We calculated a critically sampled power density spectrum for each star (ie. where the frequency resolution is inverse of the total duration of the time series data) which was fed into the detection pipeline.

For some targets, there were exceptions in how the data were processed. These targets and exceptions are described below:

- (i) For some *Kepler* targets that were previous detections, DR25 did not improve the data quality and therefore did not reveal oscillations using `pySYD`. Therefore for a subset of the sample, we used the same data as Chaplin et al. (2014). These stars are KIC IDs 2998253, 3437637, 3547794, 4465324, 4646780, 5265656, 5689219, 6034893, 6853020, 7465072, 8360349, 8656342, 10130724, 11802968, 11862119.
- (ii) For KIC IDs 6278762 and 7051180, we used pre-prepared power spectra from KASOC¹ (Handberg & Lund 2014) instead of available DR25 data from `lightkurve` due to higher noise in the data. For instance, the white noise $\nu = 6000 - 8496 \mu\text{Hz}$ is $0.6 \text{ ppm}^2/\mu\text{Hz}$ in the KASOC data, but $51 \text{ ppm}^2/\mu\text{Hz}$ in DR25 data for KIC ID 6278762. For KIC ID 7051180, the white noise is $41 \text{ ppm}^2/\mu\text{Hz}$ and $80 \text{ ppm}^2/\mu\text{Hz}$, respectively.
- (iii) For seven stars, we performed notching (ie. masking out the $l = 1$ modes) to remove mixed modes in order to measure $\Delta\nu$ confidently. These stars are primarily subgiants, KIC IDs 5683538, 5939450, 7669332, 9664694, 9894195, 10593351, 11397541.
- (iv) For KIC ID 8360349, we used only the first month of data since the photometry in the later three months was noisier. For instance, the flux scatter in the first month was ~ 140 ppm, an order of magnitude smaller than the remaining three months: ~ 1900 ppm, 3200 ppm, 1900 ppm, respectively. Similarly, for KIC ID 6106120, we used the first and tenth month of data.
- (v) For two planet hosts in Huber et al. (2013) – KIC IDs 4141376 and 5514383 – we did not find oscillations with DR25 data, and therefore used data from the original paper in Huber et al. (2013).
- (vi) For KIC ID 3861595, we used the power spectrum from the original discovery paper, Chontos et al. (2019), to confirm the detection.

2.3. Detection Pipeline

To detect solar-like oscillations and measure global asteroseismic parameters, we used `pySYD`, an open-source Python package (Chontos et al. 2022), adapted from the IDL-based `SYD` pipeline (Huber et al. 2009). While `pySYD` uses the same framework and steps as `SYD`, it has improved features such as automated background model selection, estimation of the large frequency separation with Gaussian weighting, and automated white noise calculation (Chontos et al. 2022). We briefly

¹ *Kepler* Asteroseismic Science Operations Center

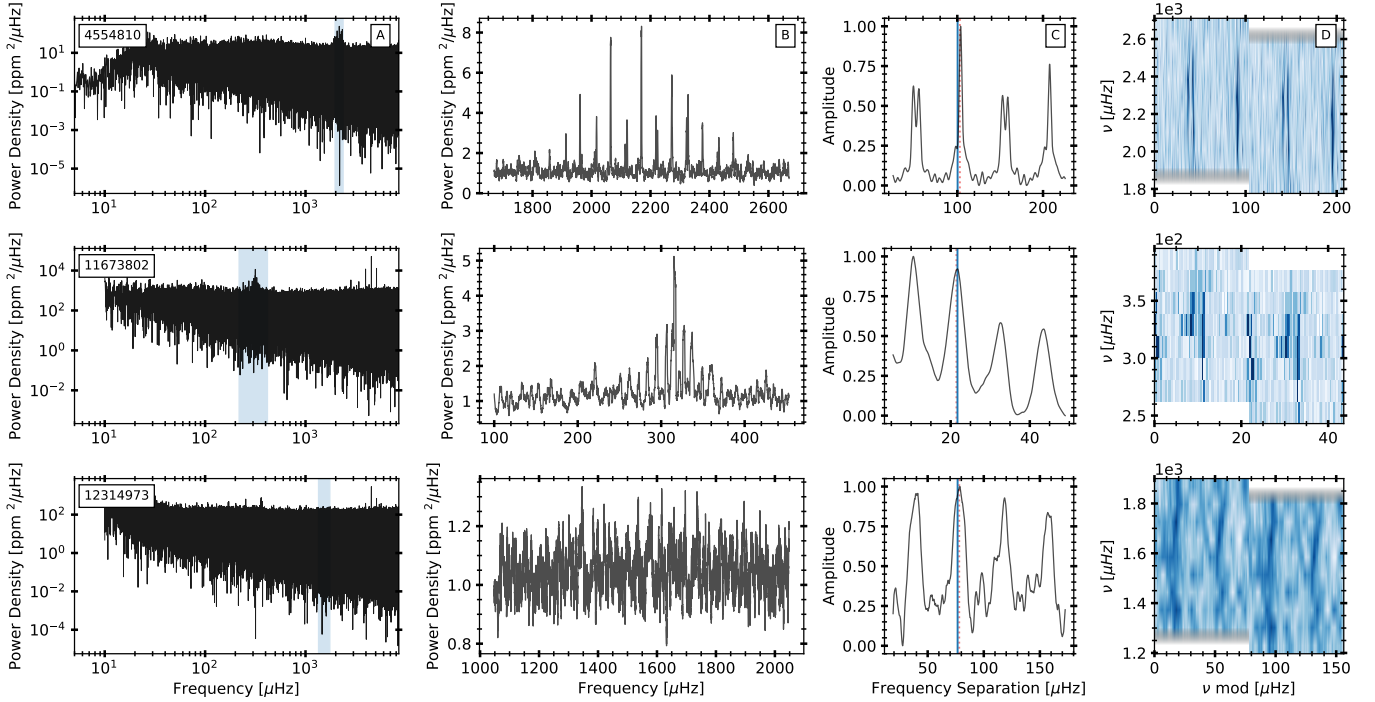


Figure 1. Example data for three *Kepler* stars with high SNR (top panels, KIC ID 4554810), moderate SNR (middle panels, KIC ID 11673802), and low SNR (bottom panels, KIC ID 12314973). *Column A:* Critically sampled power density spectrum (in units of $\text{ppm}^2/\mu\text{Hz}$). The blue band is centered on the `pySYD`'s estimated ν_{max} value. *Column B:* Background corrected power density spectrum in linear scale centered on `pySYD`'s estimate of ν_{max} . *Column C:* Auto-correlation function of the data shown in column B. The blue line corresponds to the expected $\Delta\nu$ value given the input ν_{max} , and the red dotted line corresponds to the measured $\Delta\nu$ using `pySYD`'s analysis. *Column D:* Échelle diagram of the background corrected power spectrum (shown in column B) using `pySYD`'s measurement of $\Delta\nu$.

describe the basic analysis steps of `pySYD` below, and refer the reader to [Chontos et al. \(2022\)](#) and [Huber et al. \(2011\)](#) (hereafter H11) for a more detailed discussion.

`pySYD` consists of three primary steps: (a) automatic identification of the power excess due to solar-like oscillations, (b) optimization and correction for the stellar background contribution, and (c) calculation of global asteroseismic parameters: the mean large frequency spacing ($\Delta\nu$), and frequency of maximum oscillation (ν_{max}). The pipeline first locates the region of power excess in step (a) in order to exclude this region during the background modeling and correction performed in step (b). The background, generated by granulation and stellar activity, is modelled by a sum of power laws ([Harvey 1985](#)). The frequency at which the maximum amplitude occurs in the smoothed power spectrum is taken as the frequency of maximum oscillation, ν_{max} ([Kjeldsen et al. 2008](#)). The fitted background model is then subtracted from the power spectrum in step (b), and the residual power spectrum is used to calculate the autocorrelation function (ACF) collapsed over all frequency spacings in step (c). The highest peaks in the ACF are found, and the peak closest

to the expected $\Delta\nu$ is considered the best estimate of the given target's $\Delta\nu$. Uncertainties in global asteroseismic values are estimated with Monte-Carlo simulations. Figure 1 shows data generated by `pySYD` for three stars in our sample with varying signal-to-noise.

2.4. New Detections and Comparison with Previous Results

We detected solar-like oscillations in 765 *Kepler* stars observed in short-cadence, where 50 stars are new detections and 715 are already known detections. Figures A1 and A2 in the Appendix show the smoothed, background corrected spectrum for the 50 new detections centered on ν_{max} . For all detections, Table 3 provides the *Kepler* Input Catalog (KIC) ID, source flag to indicate the original source of asteroseismic measurements, planet flag to indicate whether the star is a planet host, and seismic measurements, and Table 4 provides relevant stellar parameters for all sources. The `pySYD` output was confirmed through visual inspection, requiring a clear power excess (using an estimated ν_{max} derived with scaling relation and stellar parameters from [Berger](#)

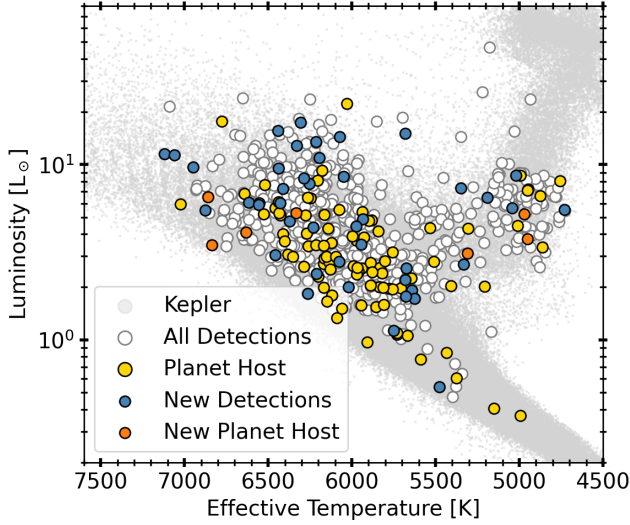


Figure 2. H–R diagram showing 765 stars with detected oscillations in white circles, new detections in blue, planet hosts in yellow, and new planet hosts in orange. The complete *Kepler* sample is shown in grey for reference, using stellar parameters from Berger et al. (2020b).

et al. (2020b)), evidence of vertical ridges in the échelle diagram, and periodic signal in the ACF. For 34 stars, the signal-to-noise is too low to report a reliable measurement of ν_{\max} from a heavily smoothed power spectrum, consistent with previous catalogs in which only $\Delta\nu$ measurements were feasible for main-sequence and subgiant oscillators (Chaplin et al. 2014). Similarly, only the ν_{\max} measurement is provided for 13 stars when $\Delta\nu$ cannot be confidently measured. Figure 2 shows the complete sample on a H–R diagram using stellar parameters from Berger et al. (2020b), derived with *Gaia* parallaxes. Our new detections are randomly distributed among the previously known sample; this is consistent with most new detections coming from the improved photometric precision of reprocessed short-cadence light curves.

We compared our global asteroseismic parameters from *pySYD* to those in literature. Most targets were found in Serenelli et al. (2017) and Chaplin et al. (2014), while other detections were found in separate studies including White et al. (2012) (KIC ID 11290197), Mosser et al. (2014) (KIC ID 6776673), Lund et al. (2017) (KIC IDs 12069424 and 12069449), Pinsonneault et al. (2018) (KIC ID 3831992), and Li et al. (2020a) (KIC ID 10920273). Published values were obtained from the most recent study; however, if a star existed in Chaplin et al. (2014) as well as a more recent study, measurements from the former were prioritized. Similarly, exoplanet hosts

with detections were published in Huber et al. (2013) (hereafter H13) and Lundkvist et al. (2016) (hereafter L16), but measurements for 40 detections were available in both catalogs; for overlapping stars, we compared our measurements to those in H13 given the similarity of the pipeline in H13 and this work. Therefore, of the 114 planet hosts observed in short-cadence, we re-analyzed all 71 in H13 and 38 in L16. Table 1 summarizes the number of stars in each catalog. See Section 2.1 for the reasoning behind the difference in the number of stars in a given catalog and those re-analyzed.

All targets in Chaplin et al. (2014) that were re-analyzed were confirmed as detections in our analysis. Two targets in Serenelli et al. (2017) (KIC IDs 3730801, 11075448), three in Mathur et al. (2022) (KIC IDs 7418476, 9109988, 10969935), and two in Balona (2020) (KIC IDs 6048403, 7833587) were not confirmed as detections. Three of these four stars had only one month of short-cadence data, which could be responsible for low data quality and difficulty in detecting oscillations.

In the sample of planet hosts from H13, we did not recover oscillations in four stars using DR25 data, but we detected oscillations in two when using data from the original paper: KIC IDs 4141376 and 5514383. The third star, KIC ID 6032981, has only one month of short-cadence data and H13 used long-cadence data to detect oscillations. For the fourth star, KIC ID 10593626, we did not recover oscillations in the DR25 data and we do not have access to the data from the original paper, Borucki et al. (2010). Similarly, there were 13 stars in L16 for which we did not find oscillations using DR25 data nor the data from the original paper: KIC IDs 4815520, 5383248, 6678383, 7887791, 7941200, 8753657, 9072639, 9579641, 10026544, 10130039, 10748390, 11600889, 11623629. Only seven had a greater than 80% detection probability while the remaining six had less than 50% detection probability. Figure A3 in the Appendix shows the power spectra of the 22 previously known detections for which we did not find solar-like oscillations. Table 5 includes the KIC IDs, source flag, and measurements of ν_{\max} and $\Delta\nu$ of the 22 targets which we did not confirm as detections.

Figure 3 compares our measurements of ν_{\max} and $\Delta\nu$ with previously measured values. We observe excellent agreement between our values and previously measured values, with an average offset of $0.2 \pm 0.7\%$ and scatter of 5.3% in ν_{\max} , and $0.2 \pm 0.4\%$ and scatter of 2.5% in $\Delta\nu$, where the scatter is the robust standard deviation of the residuals and the offset is the mean of the

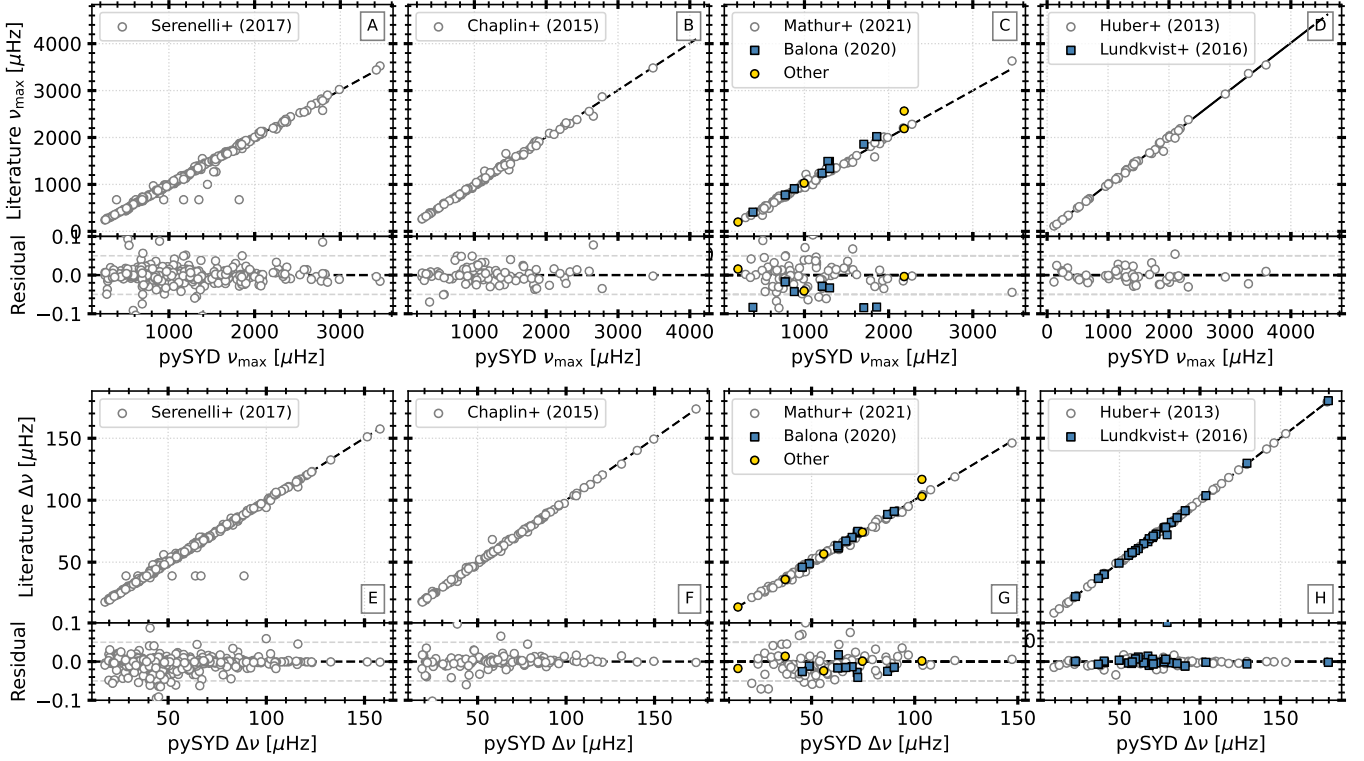


Figure 3. Comparison of ν_{\max} (top row) and $\Delta\nu$ (bottom panel) measurements from this work and previous catalogs, including Serenelli et al. (2017), Chaplin et al. (2014), Mathur et al. (2022), Balona (2020), Huber et al. (2013), Lundkvist et al. (2016), and others (summarized in Section 2.1 and Table 3). The bottom panel of each subplot shows the residuals.

residuals. We further investigated outliers² in ν_{\max} comparison between our measurements and those from Serenelli et al. (2017) (Figure 3a). There are seven³ stars with identical values of ν_{\max} in Serenelli et al. (2017) ($\nu_{\max} = 690.176 \mu\text{Hz}$) producing a collection of points horizontally, and resulting in a large deviation between our values and those published. Similarly, the outliers in Panel E of Figure 3 all have the same values of ν_{\max} and $\Delta\nu$ in Serenelli et al. (2017). In addition to these seven targets, there are additional six stars with a fraction difference greater than 10% between our measurement and those from Serenelli et al. (2017). Five of the six targets have one month of data, but the sixth target – KIC ID 5431016 – is a *F*-type star with 16 months of data. *F*-type stars show increased line widths causing the $l = 0$ and $l = 2$ modes to blend together, making it difficult to distinguish between $l = 1$ and $l = 0, 2$ modes (e.g., White et al. 2012); therefore the discrepancy between the two measurements could be caused by the broad shape of the Gaussian envelope.

² KIC IDs 4574610, 4914923, 6442183, 7341231, 7747078, 11070918, 12366681

³ KIC IDs 4641621, 5344612, 5431016, 7611858, 7910848, 8656342

2.5. Spectroscopic Activity Indicators

Stellar chromospheric activity shows indicators in the line cores of Ca II H and K, Mg II, H α and Ca infrared triplet (e.g., Hall 2008; Stassun et al. 2012). The two most popular activity indices are S_{HK} , defined as the ratio of flux in Ca II H and K lines to flux in nearby continuum region, and $\log R'_{\text{HK}}$, the ratio between chromospheric flux and bolometric flux after removal of photospheric flux, which is non-negligible for solar-like stars (e.g., Hartmann et al. 1984; Noyes et al. 1984). Compared to S_{HK} , $\log R'_{\text{HK}}$ is more appropriate for comparing Ca II H and K emission on the same scale for stars of multiple spectral types (e.g., Boro Saikia et al. 2018).

We derive S_{HK} values from publicly available spectra obtained with Keck/HIRES (Isaacson et al. 2024) using the method described in Isaacson & Fischer (2010). The spectra have an average SNR of 85 at $\approx 550 \text{ nm}$ and were in part obtained to calibrate the performance of spectroscopic analysis pipelines to derive fundamental stellar parameters (Furlan et al. 2018). We perform quality cuts to ensure reliable S_{HK} measurements, using only $S_{\text{HK}} > 0.10$ and $\text{SNR} > 8$. To calculate $\log R'_{\text{HK}}$, we require both S_{HK} and $B - V$ which can be derived

using input T_{eff} , $\log g$, and $[\text{Fe}/\text{H}]$. Although there exist methods to derive $\log R'_{\text{HK}}$ directly from S_{HK} without using T_{eff} , $\log g$, and $[\text{Fe}/\text{H}]$, we followed the method from [Noyes et al. \(1984\)](#) given its applicability across spectral types. For instance, the method described in [Lorenzo-Oliveira et al. \(2018\)](#) was calibrated on solar twins, while the one in [Marvin et al. \(2023\)](#) results in a 0.2 dex offset compared to [Noyes et al. \(1984\)](#) at low activity. We use the following relation and coefficients from [Sekiguchi & Fukugita \(2000\)](#) to derive $B - V$,

$$\begin{aligned} (B - V)_0 = & t_0 + t_1 \log(T_{\text{eff}}) + t_2 \log(T_{\text{eff}})^2 \\ & + t_3 \log(T_{\text{eff}})^3 + f_1 [\text{Fe}/\text{H}] + f_2 [\text{Fe}/\text{H}]^2 \\ & + d_1 [\text{Fe}/\text{H}] \log(T_{\text{eff}}) + g_1 \log(g) \\ & + e_1 \log(g) \log(T_{\text{eff}}) \end{aligned} \quad (1)$$

where we use T_{eff} , $\log g$, and $[\text{Fe}/\text{H}]$ from [Specmatch-synth \(Petigura 2015\)](#), a tool to extract fundamental atmospheric parameters by fitting synthetic model atmospheres from [Coelho et al. \(2005\)](#) to optical spectra.

We then use S_{HK} (on the Mount Wilson scale) and $B - V$ to derive $\log R'_{\text{HK}}$ using the updated relation from [Noyes et al. \(1984\)](#), adapted from [Middelkoop \(1982\)](#),

$$R_{\text{HK}} = 1.340 \times 10^{-4} C_{cf} S_{\text{HK}} \quad (2)$$

where $\log C_{cf} = 1.13(B - V)^3 - 3.91(B - V)^2 + 2.84(B - V) - 0.47$. However, [Noyes et al. \(1984\)](#) corrected C_{cf} for a non-physical maximum at $B - V = 0.43$, so that $\log C'_{cf} = \log C_{cf} + \Delta \log C$, where $\Delta \log C = 0$ if $B - V > 0.63$. Otherwise, $\Delta \log C$ is described by the following,

$$\begin{aligned} \Delta \log C = & 0.135x - 0.814x^2 + 6.03x^3, \\ \text{where } x = & 0.63 - (B - V) \end{aligned} \quad (3)$$

Finally, to derive $\log R'_{\text{HK}}$ from R_{HK} ,

$$\begin{aligned} \log R'_{\text{HK}} = & \log R_{\text{HK}} - \log R_{\text{PHOT}}, \\ \log R_{\text{PHOT}} = & -4.898 + 1.918(B - V)^2 \\ & - 2.893(B - V)^3 \end{aligned} \quad (4)$$

3. OSCILLATION PARAMETERS

3.1. $\Delta\nu$ - ν_{max} Relation

Our new homogeneous catalog allows us to revisit empirical relations from global oscillation parameters. Figure 4 shows the $\Delta\nu$ and ν_{max} relation for our sample. The orange solid line corresponds to the power law relation between ν_{max} and $\Delta\nu$ established for main-sequence and red giant stars ([Stello et al. 2009](#); [Hekker](#)

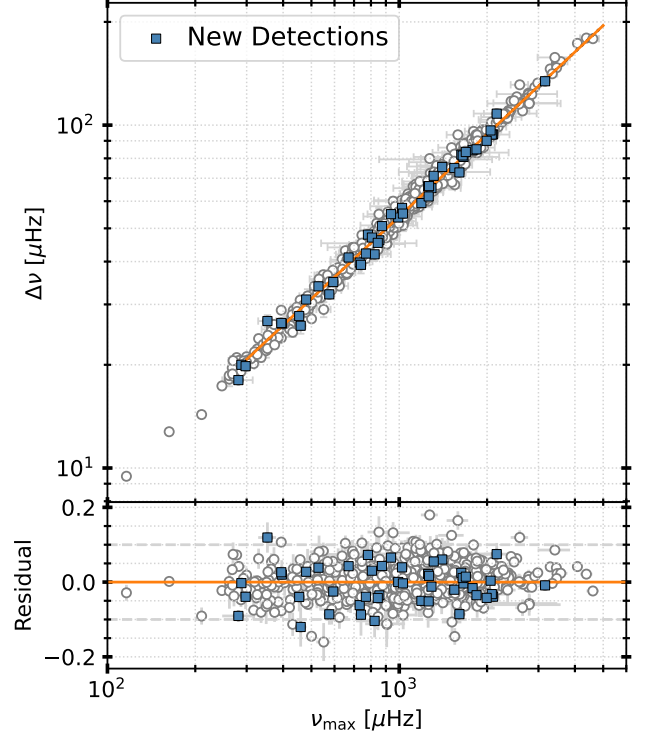


Figure 4. $\Delta\nu$ vs. ν_{max} for all 765 stars in our catalog, where the 50 new detections are shown in blue squares. The solid, orange line shows the best-fit relation between ν_{max} and $\Delta\nu$. The bottom panel shows the residuals.

et al. 2009; Mosser et al. 2010; Hekker et al. 2011a,b):

$$\Delta\nu = \alpha (\nu_{\text{max}} / \mu\text{Hz})^\beta \quad (5)$$

where $\alpha = 0.22$ and $\beta = 0.797$ for stars with ν_{max} greater than $300 \mu\text{Hz}$ (H11). We re-derive the relation and obtain similar fitting parameters: $\alpha = 0.216 \pm 0.005$ and $\beta = 0.801 \pm 0.003$, consistent with previous results. The mean offset is $0.69 \pm 0.16\%$ with a scatter of 4.4% .

As seen in the bottom panel of Figure 4, the scatter increases slightly for stars with $\nu_{\text{max}} \sim 600 - 1000 \mu\text{Hz}$. This parameter space consists of stars where the pressure modes (p -modes) and gravity modes (g -modes) overlap and create “mixed modes” ([Dziembowski et al. 2001](#)). The coupling of these two modes causes mixed modes to be shifted from their original frequency spacing, yielding multiple frequencies per radial order ([Aizenman et al. 1977](#)). Mixed modes only occur for $l > 0$ modes; since [pySYD](#) calculates the ACF over all modes (instead of just $l = 0$ modes), the estimation of $\Delta\nu$ becomes more uncertain due to the coupling of p -modes and g -modes.

The median uncertainty in ν_{max} and $\Delta\nu$ are 3.4% and 1.9% , respectively; only 14 stars have an offset

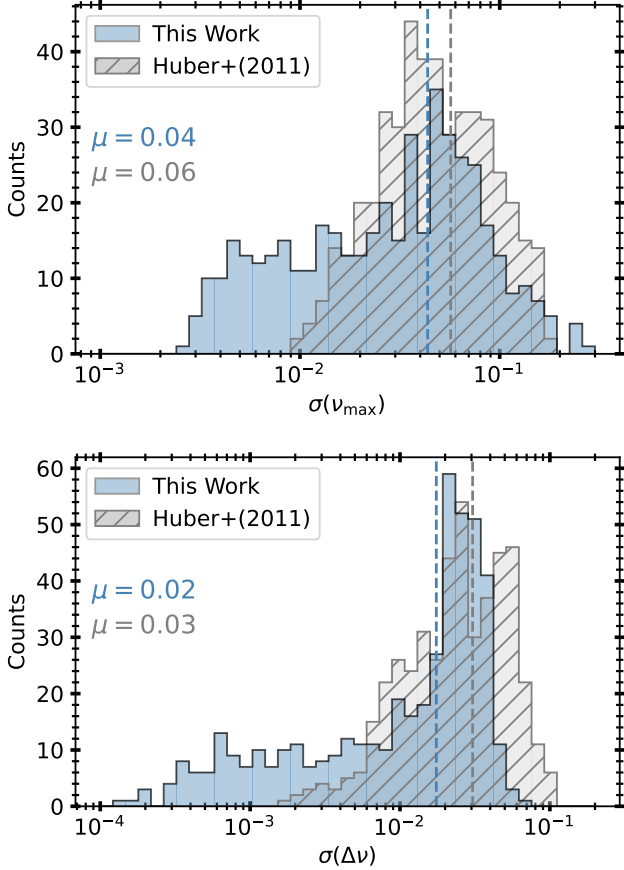


Figure 5. Fractional uncertainty in ν_{\max} (top) and $\Delta\nu$ (bottom) for 458 overlapping targets in this work (blue) and H11. The dashed lines and text indicate the mean fractional uncertainty for each sample.

greater than 10%. The 50 new detections have median uncertainty in ν_{\max} and $\Delta\nu$ of 5.0% and 2.7%, respectively. Figure 5 compares the fractional error in ν_{\max} and $\Delta\nu$ in this work with the short-cadence targets in H11. Of the 542 detections with short-cadence data in H11, 463 overlap with our sample; of the remaining 79 targets in H11 not found in our catalog, 72 are confirmed detections with long-cadence data in Yu et al. (2018) and are therefore not found in our sample by construction, and seven are non-detections. The top and bottom panels in Figure 5 show the fractional error in ν_{\max} and $\Delta\nu$, respectively. The mean error in ν_{\max} between our work and H11 is 4% and 6%, respectively, while for $\Delta\nu$ is 2% and 3%. Our measurement uncertainties in ν_{\max} and $\Delta\nu$ peak at lower values compared to those from H11. The stars with error in $\Delta\nu$ less than 0.5% have narrow peaks in the ACF that produce a small error in $\Delta\nu$; this is caused by the availability of more data: H11 only used data from Q0 – 4 while our sample contains data from all available

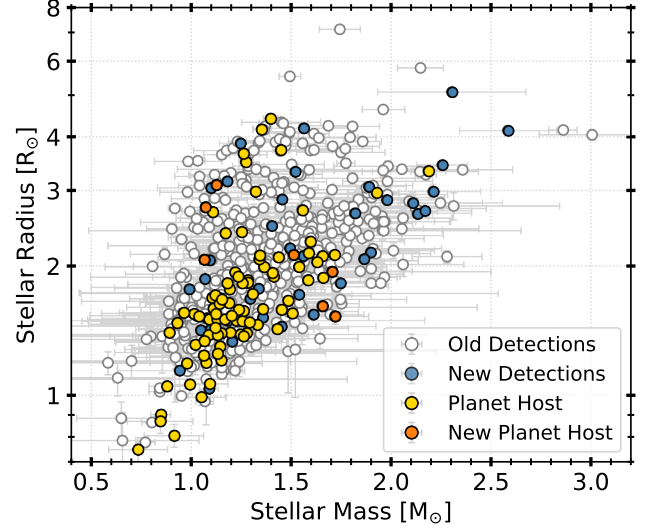


Figure 6. Derived stellar masses and radii using Equations 6 and 7 for our sample, including new detections in blue, planet hosts in yellow, and new planet hosts in orange. 70 out of 765 stars are not shown given no measurement of ν_{\max} , $\Delta\nu$, or T_{eff} .

quarters. Similarly, the 44 stars with less than 0.5% uncertainty in ν_{\max} have high resolution data (ie. the modes are clearly distinguishable in the échelle diagram) where all except for three stars had data available after Q4.

3.2. Fundamental Parameters

The global oscillation parameters ν_{\max} and $\Delta\nu$ can be combined with effective temperature to derive stellar radius and mass using the following scaling relations (Ulrich 1986; Brown et al. 1991; Kjeldsen & Bedding 1995),

$$\left(\frac{R}{R_{\odot}}\right) \simeq \left(\frac{\nu_{\max}}{\nu_{\max\odot}}\right) \left(\frac{\Delta\nu}{\Delta\nu_{\odot}}\right)^{-2} \left(\frac{T_{\text{eff}}}{T_{\text{eff}\odot}}\right)^{0.5} \quad (6)$$

$$\left(\frac{M}{M_{\odot}}\right) \simeq \left(\frac{\nu_{\max}}{\nu_{\max\odot}}\right)^3 \left(\frac{\Delta\nu}{\Delta\nu_{\odot}}\right)^{-4} \left(\frac{T_{\text{eff}}}{T_{\text{eff}\odot}}\right)^{1.5} \quad (7)$$

where $\nu_{\max\odot} = 3090 \pm 30 \mu\text{Hz}$, $\Delta\nu_{\odot} = 135.1 \pm 0.1 \mu\text{Hz}$, and $T_{\text{eff}\odot} = 5777 \text{ K}$. Values for effective temperature were obtained from Berger et al. (2020b). In Figure 6, we show the seismically derived stellar radii and masses for our sample, where 70 stars are not shown given that they do not have either ν_{\max} , $\Delta\nu$, or T_{eff} values. The median error in radius and mass is 2.7% and 10.5%, respectively, with radii between

0.7 – 7.1 R_{\odot} and masses between 0.6 – 3.0 M_{\odot} . In Figure 6, nine stars have $M < 0.8 M_{\odot}$, of which all except one have mass uncertainty above 20%. There are 18 stars with $M > 2.1 M_{\odot}$, however all except four have mass uncertainties above 5%, and 15 out of 18 have only 30 days of time-series data which could be responsible for the low data quality and uncertain asteroseismic measurements.

Asteroseismic masses and radii are sensitive to the accuracy of the effective temperatures. Since spectroscopically derived temperatures from *Specmatch* are available for a limited number of stars, we chose to use isochrone based effective temperatures from Berger et al. (2020b) in Equations 6 and 7 to ensure homogeneity. Berger et al. (2020b) validated their derived T_{eff} against interferometric and spectroscopic temperatures (see Sections 3.1 and 4.5, respectively). They found an offset of -3% to 1% when comparing to spectroscopic temperatures compiled in Mathur et al. (2017), and within 2% when compared to interferometric temperatures from Boyajian et al. (2013) and Huang et al. (2015).

In Figure 7, we compare our masses and radii with those derived from isochrone fitting using *Gaia* parallaxes from Berger et al. (2020b). The colour map represents the height-to-background ratio (HBR) of the star at ν_{max} where the height is the smoothed amplitude at ν_{max} (Mosser et al. 2012), and the background is fit with a Harvey model (Harvey 1985). Therefore, HBR is the ratio between the height and background at ν_{max} with white noise removed from the background fit,

$$\text{HBR} = \frac{H_{\nu_{\text{max}}}}{B_{\nu_{\text{max}}}} \quad (8)$$

The mean offset and error for the radius comparison (Panel A in Figure 7) is $0.8 \pm 0.2\%$ and scatter of 6% . Zinn et al. (2019) performed a similar analysis comparing the *Gaia* radii to seismic radii for main-sequence and subgiant stars, and achieved a residual median and scatter of $\sim 1\%$ and $\sim 4\%$, respectively. Although we achieve similar precision, our sample mostly contains low SNR stars, where 66% of the sample has HBR below 10. To investigate the source of outliers, we inspect the re-normalized unit weight-error (RUWE) from *Gaia* DR3. RUWE is the magnitude and colour-independent re-normalization of the astrometric χ^2 is sensitive to close binaries (e.g., Evans et al. 2018; Gaia Collaboration et al. 2018; Lindegren et al. 2018; Berger et al. 2020b; Gaia Collaboration et al. 2023). Stars with $\text{RUWE} \gtrsim 1.5$ are more likely to have a companion. Of the outliers, the star at $(R_S, R_G) \simeq (1.6, 4.3)$ is KIC ID 5513648 with a RUWE of 14 in

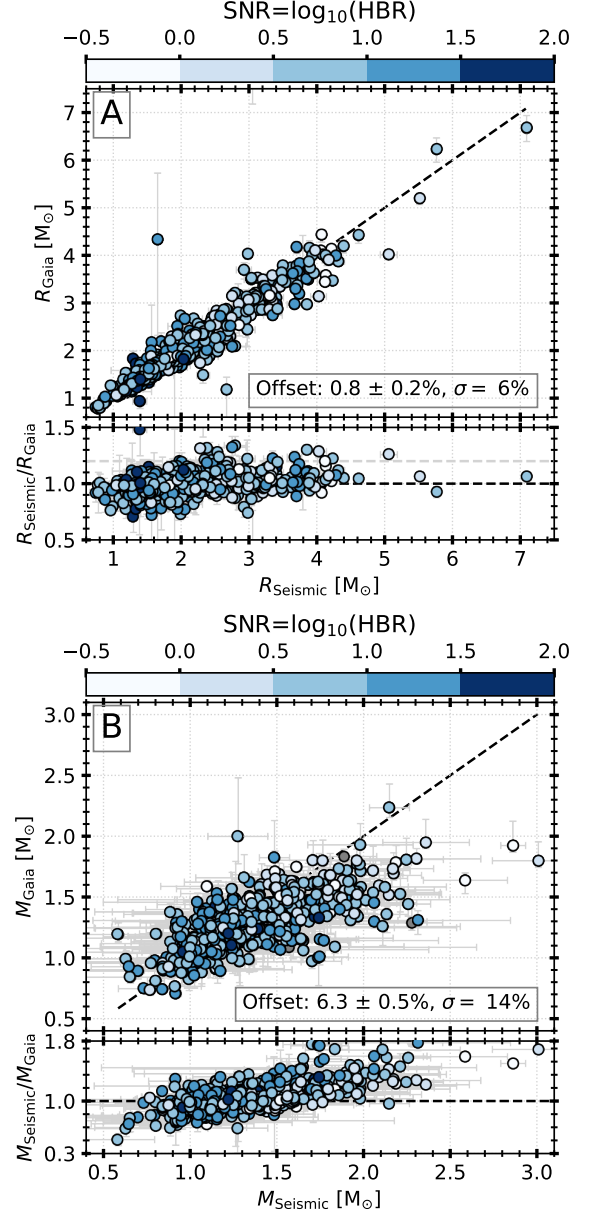


Figure 7. Comparison of radii (*top*) and masses (*bottom*) derived with asteroseismic scaling relations (x-axis) and with *Gaia* measurements (y-axis). Residuals (ie. ratio between the seismic and *Gaia* derived quantities) are shown in bottom panels. The color-coding denotes the height-to-background ratio, defined as the ratio between the amplitudes of oscillation and background. The text indicates the mean offset and error between the two measurements and the scatter, σ .

Gaia DR2 (a *Gaia* DR3 value is not available for this star), the star at $(R_S, R_G) \sim (5, 4)$ is KIC ID 6627507, a subgiant with only one month of data, and the star at $(R_S, R_G) \sim (2.6, 1.2)$ is KIC ID 6863041 with a RUWE of 4.9. There is one star outside of the plot limits,

KIC ID 11558593 at $(R_S, R_G) \sim (3.0, 8.5)$ which has a RUWE of 7.8. Three of the four stars with greater than 50% difference between the two radii have RUWE > 4.9 (the fourth star is KIC ID 5513648 and does not have a RUWE measurement in *Gaia* DR3); this suggests that the *Gaia* radii are most likely untrustworthy since the photometry will be affected by companions. Targets with an offset between 20–50% show no correlation with ν_{\max} , Kp , RUWE, effective temperature, and $\log g$. We conclude that these differences are due to the difficulty of measuring accurate radii from isochrone fitting alone.

Figure 7B compares seismic mass and masses from isochrone fitting, or *Gaia* masses. The mean offset is $6.3 \pm 0.5\%$ with a scatter of 14%, where 22% of the targets have greater than 20% offset between the seismic and *Gaia* masses; however of these, 88% have RUWE below 1.5 suggesting that contamination in the photometry is not responsible for inaccurate mass measurements. Furthermore, there is an overall trend where seismic masses are systematically higher than *Gaia* masses for our mass range as seen in the residuals. However, there is no correlation between this large offset in mass and stellar parameters (eg., T_{eff} , radii, RUWE, HBR, Kp , nor error in ν_{\max} , $\Delta\nu$, T_{eff} , or stellar mass) suggesting that masses from isochrone fitting are uncertain.

Figure 8 compares our stellar radii and masses to those estimated by the *Gaia* Final Luminosity Age Mass Estimator (FLAME) pipeline (Hidalgo et al. 2018). We used TOPCAT to match our sample to those from *Gaia* DR3 with a finding radius of $2''$. We also ensure good quality flags in the FLAME radii and masses (ie. first digit in `Flags-Flame` is 0). For our sample of 765 targets, FLAME radii and masses are available for 584 and 581 targets, respectively, as compared to 695 targets with both seismic measurements and isochrone derived radii and masses from Berger et al. (2020b). For both radius and mass, we observe distributions similar to those in Figure 7, with a mean offset of $-2.0 \pm 0.3\%$ with a scatter of 5% in radius, and a mean offset of $5.9 \pm 0.7\%$ with a scatter of 15% in mass.

3.3. Oscillation Amplitudes

We calculated oscillation amplitudes per radial mode using the following relation from Kjeldsen et al. (2008),

$$A = \sqrt{\frac{\text{PSD} \cdot \Delta\nu}{c}} \quad (9)$$

where PSD is the maximum power spectral density of the smoothed oscillation envelope in $\text{ppm}^2/\mu\text{Hz}$ returned by `pySYD` at ν_{\max} , $\Delta\nu$ is the frequency separation of the star in μHz , and c is the normalization factor of 3.04 (Kjeldsen et al. 2008; Huber et al. 2011).

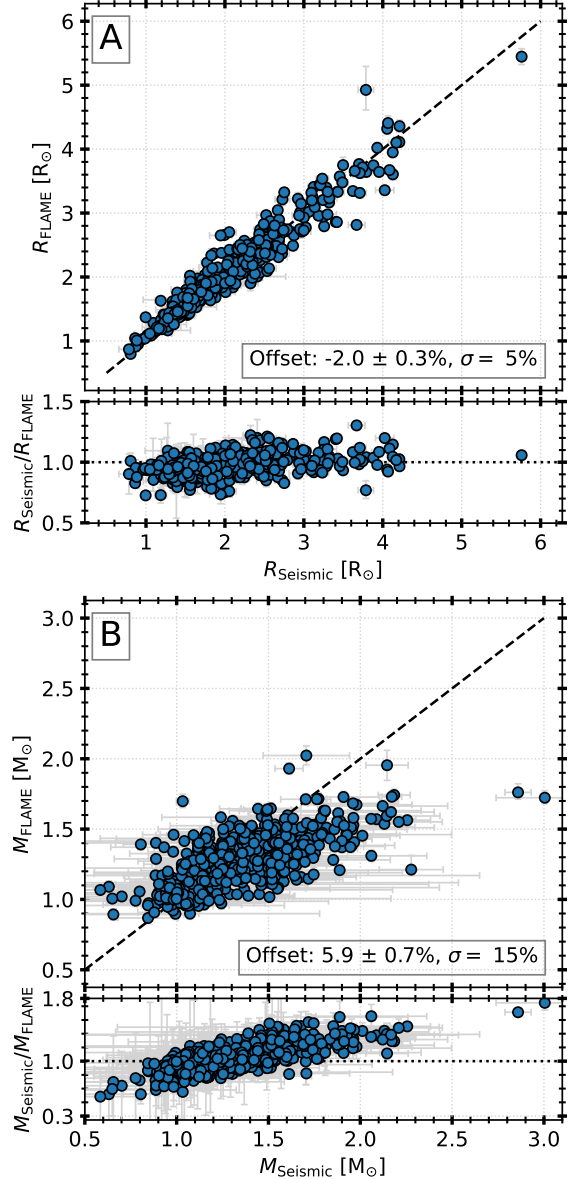


Figure 8. Comparison of radii (*top*) and masses (*bottom*) derived with asteroseismic scaling relations (x-axis) and *Gaia* DR3 FLAME measurements (y-axis). Residuals are shown in the bottom panels. The text indicates the mean offset and error between the two measurements and the scatter, σ .

Figure 9 compares our amplitude measurements to those from H11. We see a clear offset in the amplitudes from this work and H11, with mean offsets of $10.6 \pm 0.6\%$ and $13.3 \pm 1.0\%$, respectively. We suspect that these offsets are a result of improved SNR due to the longer timeseries used in this paper, and differences between the original pipeline version used by H11 and `pySYD`. Specifically, `pySYD` fits for the white noise level

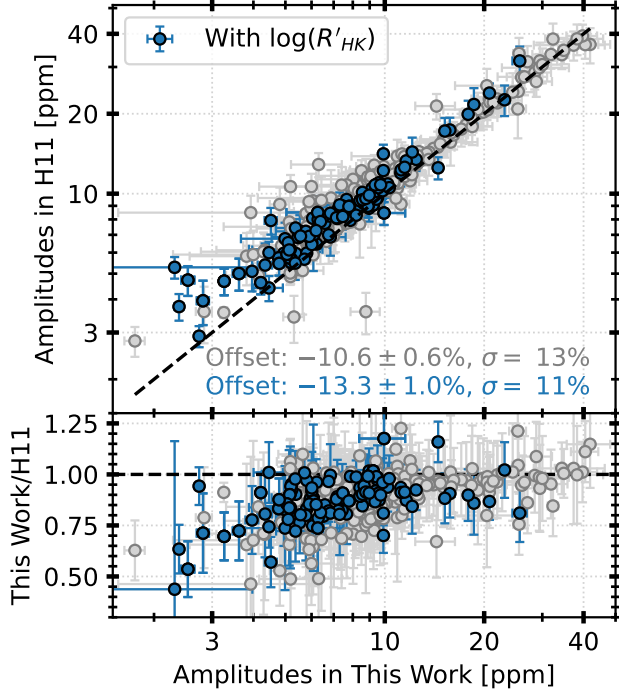


Figure 9. Comparison of amplitudes derived in this work to those from Huber et al. (2011) for 447 targets in grey. The blue points show the 132 targets for which $\log R'_{\text{HK}}$ values are available in HIRES. The text indicates the mean offset with error, and scatter in both distributions. The dashed line indicates unity. The bottom panel shows the residual.

in the background modeling step, rather than using a fixed white noise value (ie. average amplitude at high frequencies) as was used in H11. In addition, `pySYD` optimizes the specific Harvey model used where the options are ‘regular’, ‘second’, or ‘fourth’; the regular model includes the second and fourth order terms, the second model includes only the second order term, and the fourth model includes only the fourth order term. The pipeline in H11 only used the regular model with both the second and fourth order terms, and this step was therefore not optimized for each star.

In Figure 10A, we plot the observed amplitude as a function of measured ν_{max} . Note that 47 stars are missing from this plot given no measurement of ν_{max} or $\Delta\nu$. The star at $(\nu_{\text{max}}, A_{\text{obs}}) \sim (100, 17)$ – KIC ID 6470149 – has a clear oscillation pattern, but its low resolution makes the ν_{max} measurement difficult and could be responsible for its deviation from the distribution. Similarly, KIC ID 9390670 at $(\nu_{\text{max}}, A_{\text{obs}}) \sim (1304, 2.3)$ is a low SNR detection with an uncertain ν_{max} , and a greater than 50% error in observed

amplitude. The observed change in slope at $\sim 1500 \mu\text{Hz}$ is consistent with previous studies (e.g., H13).

Similar to previous studies (e.g., H11), the amplitude– ν_{max} relation shows significantly more scatter than expected from measurement errors. To investigate possible correlations with other parameters, Figure 10B shows the same distribution coloured by the metallicity for each star, where spectroscopic metallicities are available for 73% of our sample from three sources: Bruntt et al. (2012); Buchhave & Latham (2015); Serenelli et al. (2017). We find no gradient or pattern for main-sequence and subgiant stars in this parameter space. This is similar to the results from Yu et al. (2018) for red giant stars, but different than their results for red clump stars, where they found that metal-rich red clump stars oscillate with larger amplitudes than metal-poor stars at a given ν_{max} , $\Delta\nu$, and T_{eff} (see Figure 12 in Yu et al. (2018)).

Figure 10C shows the distribution colour-coded by Kp , with the lack of correlation confirming that the spread is not due to an inaccurate white noise correction. In Figure 10D, we show the relationship between RUWE from *Gaia* DR3 and amplitude at ν_{max} . In our sample, 122 stars (or 17% of the sample) have RUWE above 1.5 which are coloured in Figure 10D. A close companion would dilute the amplitude (due to extra light), which could yield an underestimated amplitude, where low amplitude corresponds to higher stellar activity (e.g., Chaplin et al. 2000; Komm et al. 2000; Chaplin et al. 2011a). As seen in Panel D, stars with $\text{RUWE} \geq 1.5$ follow the overall distribution of our sample with no outliers. Figure 10E shows the relationship between seismic mass and amplitude, where mass is derived using Equation 7. We find that lower mass stars have higher amplitude at a given ν_{max} on average while the opposite is true for higher mass stars, consistent with H11 and Yu et al. (2018). Lastly, Figure 10F shows no correlation between effective temperature and amplitude at a fixed ν_{max} .

3.4. A New Oscillation Amplitude Scaling Relation including Chromospheric Activity

H11 derived a scaling relation to predict oscillation amplitude given stellar mass, radius, and temperature. We revise their scaling relation by including available chromospheric activity measurements for our sample. To do this, we derive a modified amplitude scaling relation including the $\log R'_{\text{HK}}$ term normalized to solar $\log R'_{\text{HK}}$ value of -4.94 (Egeland et al. 2017),

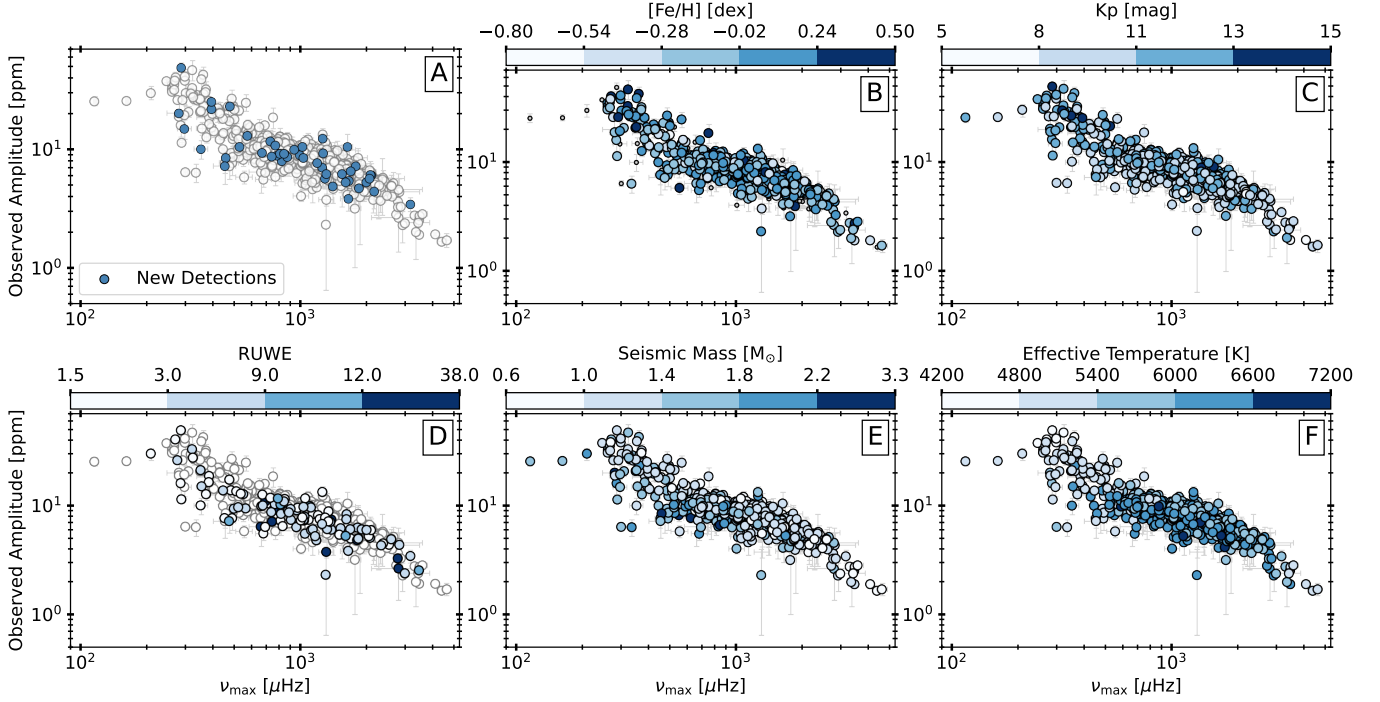


Figure 10. Observed amplitude at ν_{\max} as a function of frequency of maximum oscillation. Panel A shows the new detections in blue against the overall sample in grey. Panels B–F are coloured by stellar properties: metallicity (B), K_p (C), *Gaia* DR3 $\text{RUWE} \geq 1.5$ (D), seismic mass (E), and *Gaia* effective temperature from Berger et al. (2020b) (F).

$$\frac{A}{A_{\odot}} = \frac{L^s (\log(R'_{\text{HK}}) / \log(R'_{\text{HK}})_{\odot})^u}{M^t T_{\text{eff}}^{r-1} c_K(T_{\text{eff}})}, \quad c_K = \left(\frac{T_{\text{eff}}}{5934} \right)^{0.8} \quad (10)$$

where the solar reference amplitude A_{\odot} is 3.6 ppm, and c_K is the bolometric correction factor as a function of effective temperature (Ballot et al. 2011).

We re-derived the solar reference values for *pySYD* following H11 by using 112 30-day subsets of data from the VIRGO instrument (Fröhlich et al. 1997), after processing the data following methods described in Section 2.2. We measure a mean oscillation amplitude of 4.57 ± 0.33 ppm, $\nu_{\max} = 3080 \pm 30$ μHz , and $\delta\nu = 135.1 \pm 0.1$ μHz . Given VIRGO’s green channel ($\lambda = 500$ nm), we convert our measured amplitude to a solar bolometric amplitude of 3.66 ± 0.27 ppm using methods outlined in Kjeldsen & Bedding (1995). Our reference values are consistent with H11 and the solar amplitude from Michel et al. (2009), so we continue to use $A_{\odot} = 3.6$ ppm in the following analysis for consistency.

To predict amplitudes, we use asteroseismic radii and masses derived with both photometric T_{eff} from Berger et al. (2020b), and spectroscopic T_{eff} from *Specmatch*. Table 6 includes spectroscopic parameters (T_{eff} , $\log g$, $[\text{Fe}/\text{H}]$), $B - V$, $\log R'_{\text{HK}}$, $\sigma(\log R'_{\text{HK}})$ and

re-derived seismic masses and radii for 127 stars. We estimate uncertainties on $\log R'_{\text{HK}}$ via bootstrapping by perturbing the spectroscopic quantities with typical uncertainties. For the S -index, we assume a typical uncertainty of 1.6% as found by Gomes da Silva et al. (2021). The mean relative uncertainty in $\log R'_{\text{HK}}$ is therefore 3%, similar to Gomes da Silva et al. (2021).

There is an offset of $0.5 \pm 0.1\%$ between the isochrone derived T_{eff} from Berger et al. (2020b) and *Specmatch* T_{eff} , with a scatter of 1.9%. Of the 172 stars with available $\log R'_{\text{HK}}$ values, $T_{\text{eff,iso}}$, and $T_{\text{eff,spec}}$, 40 stars (or 23% of the sample) have $\Delta T_{\text{eff}} > 100$ K, but 14 of them are hot stars, with $T_{\text{eff,iso}} > 6400$ K. On average, the difference between the two T_{eff} measurements is 31 K.

We limit our sample to targets between $A_{\text{obs}} = [4, 20]$ ppm, and use both spectroscopic T_{eff} from *Specmatch* ($T_{\text{eff,spec}}$) and isochrone based T_{eff} from Berger et al. (2020b) ($T_{\text{eff,iso}}$) in Equation 10 to calculate expected amplitudes. In Figure 11, we show the results from spectroscopic T_{eff} in the top panel and isochrone based T_{eff} in the bottom panel for 127 stars. In the left panel of Figure 11, we derive the expected amplitudes with our observed amplitudes and H11 scaling relation, similar to Equation 10, but without the $\log R'_{\text{HK}}$ term (e.g., $u = 0$). We compare the best-

Table 2. Best-fit parameters in Equation 10 using the old scaling relation from H11 without the activity term (ie. $u = 0$ in Equation 10) and the new scaling relation with the activity term. The mean offset with error, scatter, and BIC (Equation 11) is included for both models for reference. The best-fit parameters are listed using both spectroscopic and isochrone based effective temperatures, $T_{\text{eff, spec}}$ and $T_{\text{eff, iso}}$.

	Model	
Parameter	H11 Relation	New Relation
Best Fit Parameters with $T_{\text{eff, spec}}$		
r	2.319 ± 0.040	2.986 ± 0.043
s	0.861 ± 0.004	0.682 ± 0.006
t	1.572 ± 0.021	0.985 ± 0.025
u	0	3.122 ± 0.081
Offset	-2.90 ± 1.10	-1.65 ± 0.86
Scatter	12%	9%
BIC	89.2	73.3
Best Fit Parameters with $T_{\text{eff, iso}}$		
r	2.555 ± 0.036	3.053 ± 0.038
s	0.864 ± 0.004	0.691 ± 0.006
t	1.553 ± 0.020	1.013 ± 0.024
u	0	3.129 ± 0.077
Offset	-3.11 ± 1.06	-1.69 ± 0.79
Scatter	11%	8%
BIC	86.1	68.4

fit parameters from H11 (grey points), with new best-fit parameters derived using an optimization routine. The new best-fit parameters with $T_{\text{eff, spec}}$ and $T_{\text{eff, iso}}$ are shown in Figure 11 left panel and listed in the first column in Table 2; both sets of best-fit parameters are similar to those in H11: $r = 2$, $s = 0.838 \pm 0.002$, and $t = 1.32 \pm 0.02$.

In the middle panel of Figure 11, we derive expected amplitudes for main-sequence and subgiant stars ($T_{\text{eff}} \in [4900, 6700]$ K, $\log g \in [3.2, 4.5]$ dex, and $\log R'_{\text{HK}} \in [-5.6, -4.8]$) with four fit parameters, r , s , t , and u . The best-fit parameters are listed in the right column of Table 2. There are eleven stars⁴ with greater than 25% offset between the expected and observed amplitudes using both $T_{\text{eff, spec}}$ and $T_{\text{eff, iso}}$. Two stars (KIC ID 7510397 and 3123191) have RUWE above 1.5, while the remaining stars have RUWE below 1.1. These targets

show no correlation between their seismic and stellar parameters (ie. ν_{max} , $\Delta\nu$, T_{eff} , Kp , P_{rot} , $[\text{Fe}/\text{H}]$, HBR) and their large offset.

In the right panel of Figure 11, we compare the new scaling relation in this work with the relation and best-fit parameters from H11, and relation from H11 but re-derived best-fit parameters. Using the new relation, we achieve an average offset of $-1.65 \pm 0.86\%$ and scatter of $\sigma = 9\%$ with $T_{\text{eff, spec}}$, and $-1.69 \pm 0.79\%$ and $\sigma = 8\%$ with $T_{\text{eff, iso}}$. Using H11 relation and best-fit parameters, we obtain an offset of $-2.90 \pm 1.10\%$ and scatter of $\sigma = 12\%$ with $T_{\text{eff, spec}}$, and $-3.11 \pm 1.06\%$ and $\sigma = 11\%$ with $T_{\text{eff, iso}}$. A possible source of scatter could be caused by the metallicity and temperature dependence on c in Equation 9 (Ballot et al. 2011), as well as ignoring the metallicity dependence on the bolometric correction (Lund 2019).

We calculated the Bayesian Information Criterion (BIC) to compare amplitude scaling relation models:

$$\text{BIC} = n \ln \left(\frac{\text{RSS}}{n} \right) + k \ln(n) \quad (11)$$

where the likelihood function is the mean squared error (the residual sum of squares (RSS) divided by number of data points), n is the number of data points, and k is the number of free parameters (Priestley 1981; Hastie et al. 2001). For the new relation, $k = 4$, but $k = 3$ for the old scaling relation. We calculate $\delta_{\text{BIC}} = 15.9$ for $T_{\text{eff, spec}}$ and $\delta_{\text{BIC}} = 17.7$ with $T_{\text{eff, iso}}$, providing significant evidence in favor of the new model (Raftery 1995).

We conclude that the new scaling relation with the activity term is more successful at recovering observed oscillation amplitudes with a lower offset and scatter. The modest improvement compared to the old scaling relation is likely due to measurement uncertainties in the amplitudes, which are now comparable to the residual scatter ($\approx 10\%$). Our results of an improved oscillation amplitude with an addition of an activity term is similar to results found by Campante et al. (2014); they tested two models to predict oscillation amplitude and found that the model with a magnetic activity proxy performed better the model without. Similarly, Bonanno et al. (2019) proposed a new amplitude-luminosity relation with spot fraction as a proxy for magnetic activity using data from subgiant EK Eri; however, while their new expected amplitude improved, it was still under-predicted by a factor of six, and calibrated on one target only.

4. DISCUSSION

⁴ KIC IDs 3123191, 3967859, 5856836, 7510397, 7510397, 8018599, 8420801, 8561221, 11389437, 11389437, 11453915

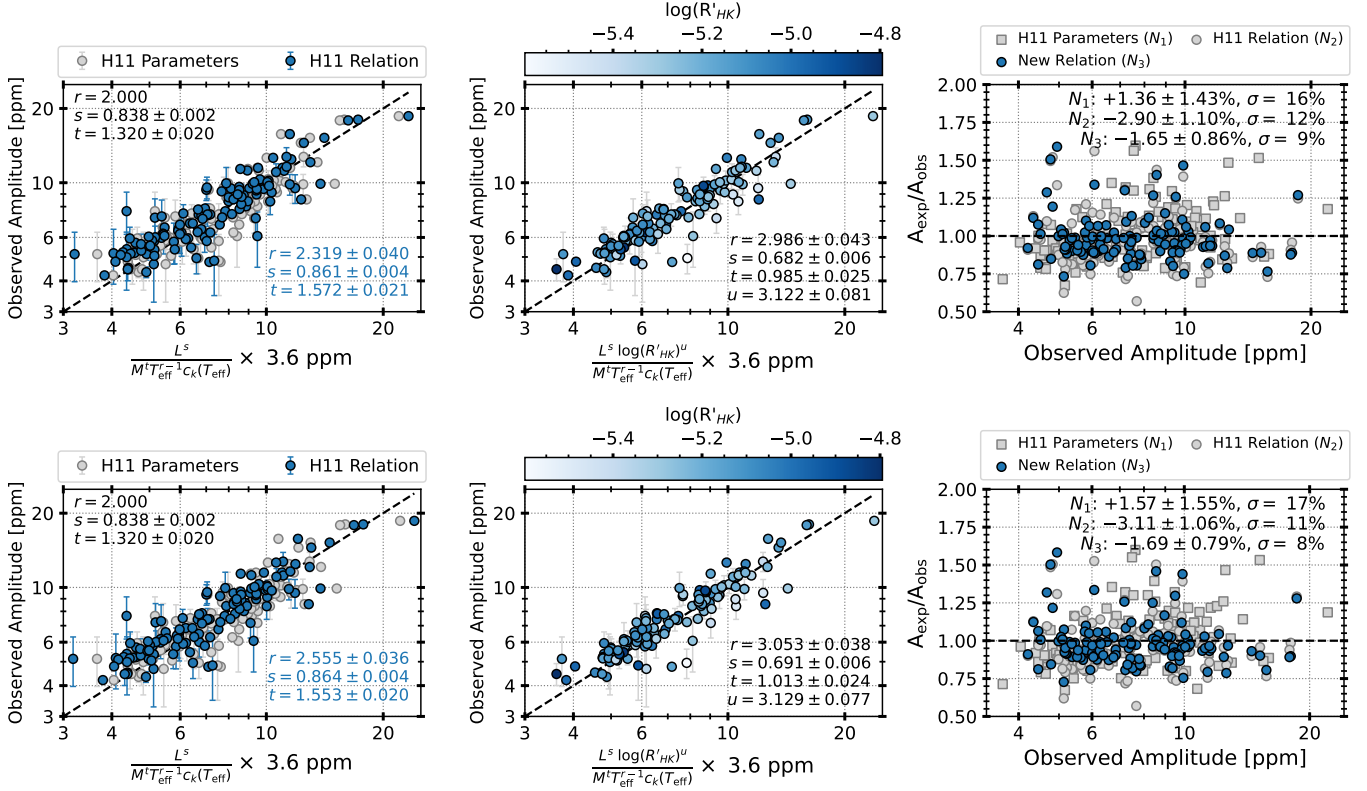


Figure 11. Amplitude scaling relations derived with spectroscopic T_{eff} from *Specmatch* (top panels) and isochrone based T_{eff} from *Berger et al. (2020b)* (bottom panels). *Left:* Observed amplitude as a function of the expected amplitude derived using Equation 10 without an activity term. The grey points show the expected amplitudes using best fit parameters from H11 and the blue points show the expected amplitudes with the relation from H11 but with new best-fit parameters, r , s , and t . The dashed line shows the one-to-one relation. The text indicates the best-fit parameters for both distributions. *Middle:* Same as left panel but including an activity term, coloured by the $\log R'_{\text{HK}}$ index from *HIRES*. The annotated text indicates the best-fit parameters, and the dashed line shows the one-to-one relation. *Right:* Residuals between observed and predicted amplitudes using the relation and best-fit parameters from H11 (grey circles), the expected amplitudes derived using H11 relation but re-derived best-fit parameters (grey squares), and the new relation from Equation 10 (the blue circles). The annotated text indicates the mean offset with error and the scatter.

4.1. Exoplanet Host Stars

We searched for solar-like oscillations in all *Kepler* stars with short-cadence data including those that were given an exoplanet disposition of confirmed or candidate on the NASA Exoplanet Archive. Given the selection criteria, we also included any exoplanet hosts that were also classified as binaries in *Kirk et al. (2016)*; 65 targets satisfied this criterion. We confirmed solar-like oscillations in 94 of the 110 previously known detections (69 out of 71 in H13, 25 out of 38 in L16, and 1 in *Chontos et al. (2019)*).

We also discovered solar-like oscillations in seven new KOIs: KIC ID 2162635 (KOI 1032), 3662838 (KOI 302, *Kepler-516*), 5897826 (KOI 126, *Kepler-469*), 6462863 (KOI 94, *Kepler-89*), 7730747 (KOI 684), 9955262 (KOI 76), and 11074835 (KOI 2533, *Kepler-1270*). The background corrected power spectrum for the seven new

detections is shown in Figure 12. The power spectra for the 15 planet hosts which we did not confirm as detections are shown in Figure A3; two targets are from H13 and 13 targets are from L16.

Using our revised stellar radii, we re-derived planet radii as follows,

$$R_p = \frac{R_{p,V}}{R_{s,V}} \times R_{s,\text{seismic}} \quad (12)$$

$R_{p,V}$ and $R_{s,V}$ are planet radius and stellar radius from *Van Eylen et al. (2018)* (hereon VE18), and $R_{s,\text{seismic}}$ is seismically derived stellar radii in this work. VE18 contains 75 stars hosting 117 planets. Our catalog contains 108 planets around 67 host stars; of the remaining 9 planets not found in our catalog, 7 are around hosts not confirmed as detections in this work, one target does not have short-cadence data available (KIC ID 9642292, *Kepler-1392*), and one planet is now

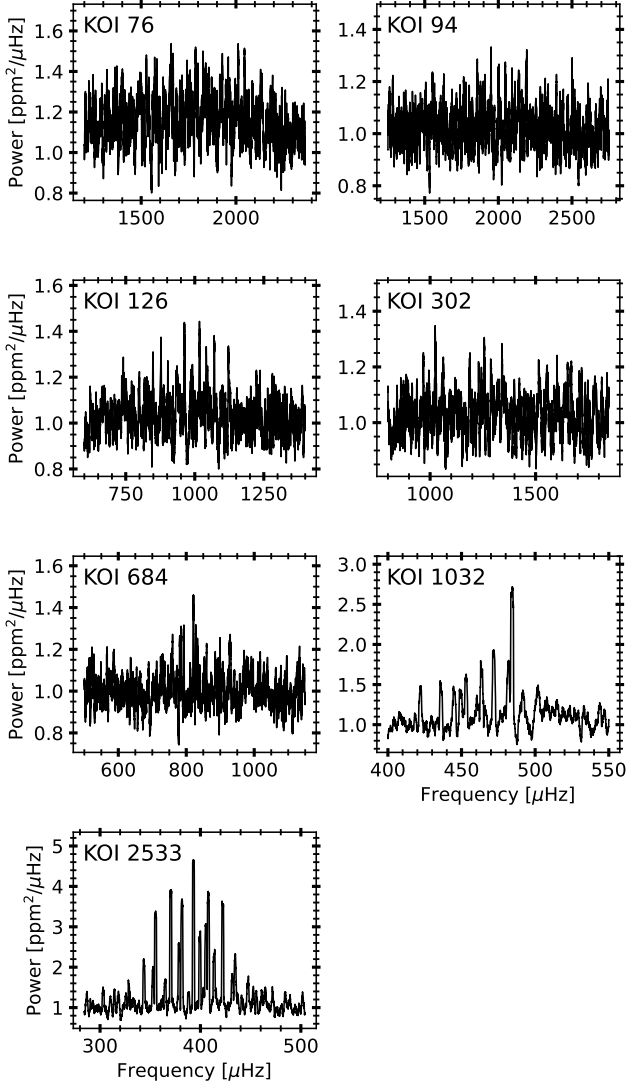


Figure 12. Background divided power spectra for seven *Kepler* hosts with newly discovered oscillations centered on ν_{\max} .

labeled as a false positive (KOI-5c). Furthermore, while 64 hosts from VE18 are also found in our catalog, five do not have stellar radius measurement available, due to no measurement in ν_{\max} , $\Delta\nu$, or T_{eff} . Therefore, we compare planet radii for 98 planets around 62 hosts to those from VE18.

Figure 13A shows the ratio between the planet radii derived using our stellar radii and planet radii from VE18. The mean offset is $1.4 \pm 0.4\%$ with a scatter of 4%, suggesting good agreement between the two samples. The mean error in planet radius as found by VE18 is 3.9%, while the mean error in planet radius derived using Equation 12 is 6.1%.

Figure 13B shows the planet radii on a period–radius plane, with orbital periods obtained from VE18, and

Figure 13C shows the distribution of seismically derived planet radii and those from VE18. We observe a gap in the radius distribution at $R \approx 2 R_{\oplus}$, consistent with the radius valley, a feature in the demographics of short-period ($P < 100$ days) planets with radii between $1.3 - 2.6 R_{\oplus}$ (Owen & Wu 2013; Fulton et al. 2017). Our distribution is similar to VE18 who investigated the radius valley using accurate stellar parameters from asteroseismology, and also consistent with previous studies (e.g., Owen & Wu 2013; Jin et al. 2014; Lopez & Fortney 2014; Chen & Rogers 2016; Owen & Wu 2017; Lopez & Rice 2018; Van Eylen et al. 2018; Berger et al. 2020a). Leading theories to explain the radius valley include photoevaporation (Owen & Wu 2017), core-powered mass-loss (Ginzburg et al. 2016, 2018), and gas-poor formation (Lee et al. 2022). Similar to VE18, we find no planets within the gap using the stellar radii derived in this work, supporting the theory that previous “gap planets” are caused by uncertainties when constraining impact parameters without precise mean densities and short-cadence data (Petigura 2020).

4.2. Gyrochronology

Stellar ages are difficult to measure for low-mass stars, which are generally not amenable to age dating using isochrones or asteroseismology (Soderblom 2010). Gyrochronology is a powerful method to empirically determine stellar ages relying only on stellar rotation periods (e.g., Barnes 2007; Mamajek & Hillenbrand 2008; Angus et al. 2015, 2019; Spada & Lanzafame 2020). Most gyrochronology relations have been calibrated on nearby, young open clusters, and therefore are limited for older stars (e.g., Meibom et al. 2015). Furthermore, the current sample of rotation periods in *Kepler* is biased since periods are measured for active stars that produce flux variations in the photometry, but stellar activity decreases for older stars (Skumanich 1972). Calibration of these relations is required for confident age determination, but so far has produced discrepancies between clusters, *Kepler* stars, and nearby field stars (e.g., Angus et al. 2015).

In addition, the unexpected rapid rotation of stars more evolved than the Sun, a phenomenon known as weakened magnetic braking, has tested the accuracy of past age–rotation relations (e.g., van Saders et al. 2016; Hall et al. 2021; Metcalfe et al. 2022; Bhalotia et al. 2024). Fortunately, rotation rates as measured with rotational splitting of asteroseismic oscillation frequencies can help to calibrate age–rotation relation for older stars. It is therefore prudent to expand the sample of solar-like oscillators with high signal-to-

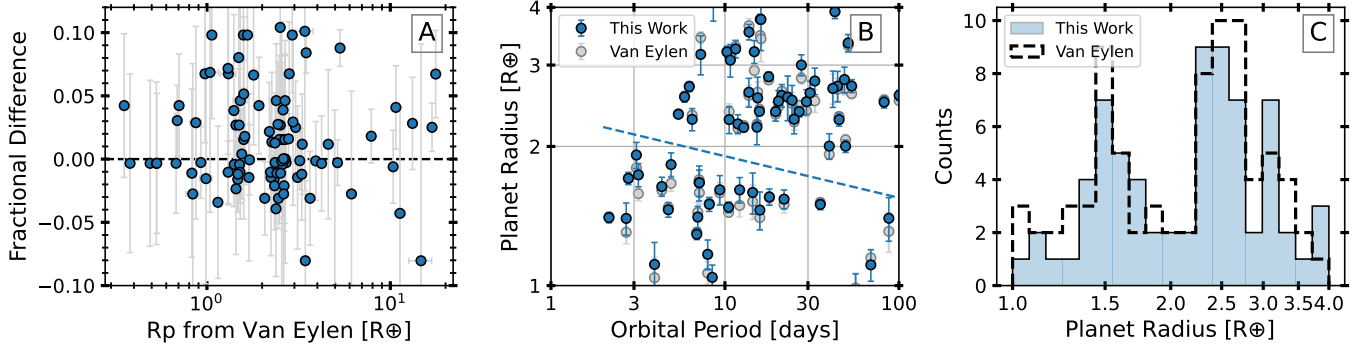


Figure 13. *Panel A:* Fractional difference between planet radii from asteroseismology and those from Van Eylen et al. (2018) (VE18): $(R_{p, \text{this work}} - R_{p, \text{VE18}})/R_{p, \text{VE18}}$. *Panel B:* planet radii on period-radius plane, where the grey and blue points are planet radii from VE18 and asteroseismology, respectively, and dashed line indicates the radius valley, with best-fit parameters ($m = -0.09$ and $\alpha = 0.37$) and axes limits from VE18. *Panel C:* distribution of planet radii from asteroseismology (blue), and from VE18 (dashed black).

noise for calculating age, and calibrating rotation-age relations for older stars.

Figure 14 shows our sample with rotation periods and effective temperatures from Berger et al. (2020b) against the complete sample from Santos et al. (2021) for reference. Rotation periods were obtained from Santos et al. (2021) (266 stars), McQuillan et al. (2014) (52), García et al. (2014) (91), and Hall et al. (2021) (37). The group of detections at ~ 5500 K above the Santos et al. (2021) distribution is because the asteroseismic sample is biased towards subgiants. Of the 451 stars with rotation periods, 11 (not including targets from Silva Aguirre et al. (2015) and Silva Aguirre et al. (2017)) have sufficiently high data resolution – as indicated by clear ridges in the échelle diagram – to perform detailed modeling of oscillation modes for age determination (e.g., Metcalfe et al. 2014; Creevey et al. 2017).

4.3. Comparison to Non-Detections

To test the reliability of our catalog, we compared the sample of detections and non-detections against metrics that should correlate with the probability of finding oscillations in a star (e.g., Chaplin et al. 2011b). This includes the probability of detection (see Section 2.1.1 in Bhalotia et al. (2024)), white noise, and *Kepler* apparent magnitude (Kp). In Figure 15A, we show the white noise in the power spectrum (average power at frequencies 7000 – 8500 μHz) as a function of *Kepler* apparent magnitude for both detections and non-detections. We notice no detections fainter than $Kp \sim 14$. Figure 15B shows the white noise as a function of length of time-series; while there are also many detections with short time-series, they are relatively less noisy than non-detections, with noise below ~ 1000 ppm²/ μHz . Figure 15C shows the white

noise as a function of probability of detection. Detection probabilities were calculated based on the method by Chaplin et al. (2011a), using updated *Gaia*–derived stellar parameters from Berger et al. (2020b). Most stars ($\sim 93\%$) with detected oscillations have probability greater than 80%. The 21 detections ($\sim 3\%$ of the sample) with probability below 50% are smaller stars ($R \lesssim 2 R_{\odot}$, $\log g \gtrsim 4$ dex), and have an average noise level three times smaller than detections with probability above 50%.

We further investigated non-detections with an expected probability greater than 80%, but found no common factor in stellar parameters for these stars. Stars with high probabilities that do not show detectable signal may have higher stellar activity, which is known to suppress oscillation amplitudes as investigated in Section 3.4 (e.g., Chaplin et al. 2011b), but is not taken into account when calculating detection probability. Alternatively, noise in the light curve can also be a contributing factor.

5. CONCLUSION

We have created a homogeneous catalog of asteroseismic detections in *Kepler* short-cadence data. We use pySYD to measure global asteroseismic quantities, and find solar-like oscillations in 765 stars, of which 101 are planet hosts. We provide a homogeneous catalog with global asteroseismic properties such as ν_{max} , $\Delta\nu$, amplitude of oscillation, white noise, and height-to-background ratio. We also provide stellar radii and masses derived from scaling relations, and other stellar properties such as *Kepler* magnitude, effective temperature, *Gaia* DR3 RUWE, metallicity, and rotation period. Below is a summary of our main findings:

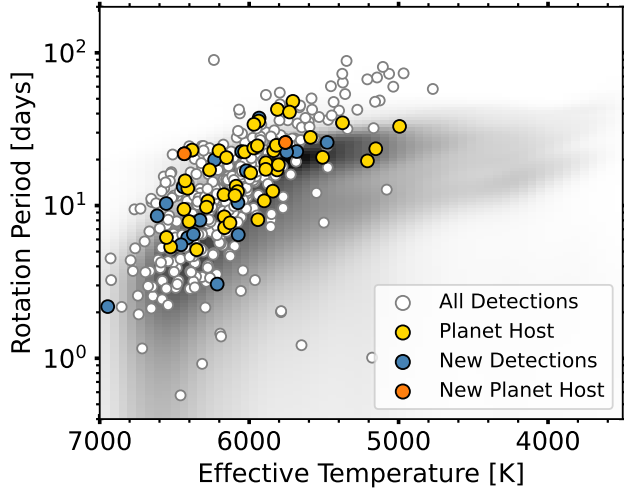


Figure 14. Rotation periods as a function of effective temperatures for all detections (unfilled points), including new detections (blue), planet hosts (yellow), and new planet hosts (orange). The complete sample from Santos et al. (2021) is shown for reference as a density distribution.

1. We find 50 new detections in the re-processed *Kepler* data, with a median uncertainty of 5.0% and 2.7% in ν_{\max} and $\Delta\nu$, respectively. The new detections have no preferential location in the H-R diagram.
2. For 765 stars, we measure ν_{\max} and $\Delta\nu$ with median uncertainty of 3.4% and 1.9%, respectively. We also derive seismic radii and masses with errors of 2.7% and 10.5%, respectively. The mean offset between our seismically derived radii and *Gaia* radii from Berger et al. (2020b) is $0.8 \pm 0.2\%$ with a scatter of 6%.
3. We re-derive the amplitude scaling relation including a term for chromospheric activity, $\log R'_{\text{HK}}$ for main-sequence and subgiant stars ($T_{\text{eff}} \in [4900, 6500]$ K, $\log g \in [3.5, 4.5]$ dex, and $\log R'_{\text{HK}} \in [-5.4, -4.9]$). Compared to the scaling relation from Huber et al. (2011), the new scaling relation slightly reduces the offset between expected and observed oscillation amplitudes, and is statistically preferred when using a photometric temperature scale. The scatter in expected amplitude of 8–9% as compared to the amplitude uncertainty of 11% suggests that most, if not all, of the scatter in the expected amplitudes can be explained by measurement uncertainty. The revised scaling relation suggests that activity indicators can be used to predict oscillation amplitudes for future surveys.

4. We find seven new detections that are *Kepler* planet hosts – KOI 1032, KOI 302 or Kepler-516, KOI 126 or Kepler-469, KOI 94 or Kepler-89, KOI 684, KOI 76, and KOI 2533 or Kepler-1270 – for which we provide global seismic parameters with detected oscillations. We derive planet radii using seismic stellar radii; the mean offset between our planet radii and those from Van Eylen et al. (2018) is $1.4 \pm 0.4\%$.
5. In the final catalog, we include previously measured rotation periods for 451 stars, where 11 have sufficiently high signal-to-noise for age determination with detailed modeling. We also provide global asteroseismic measurements for 101 planet hosts.

Our work presents the largest and most homogeneous catalog of solar-like oscillations in *Kepler* main-sequence and subgiant stars to date. Such catalogs are important for the development of data analysis tools, as benchmark stars for calibrating more indirect methods of determining stellar parameters (e.g. Furlan et al. 2018; Sayeed et al. 2021), and for improving our understanding of stellar populations in the Galaxy (e.g., Chaplin et al. 2011c). The TESS mission has already revealed hundreds of main-sequence and subgiant stars with solar-like oscillators (e.g., Chontos et al. 2021; Huber et al. 2022; Hatt et al. 2023; Metcalfe et al. 2023; Hon et al. 2024; Zhou et al. 2024). Insights and discoveries from TESS will shape science from the upcoming PLATO Mission (Rauer et al. 2014, 2024) and the Nancy Grace Roman Telescope (Spergel et al. 2015; Akeson et al. 2019), which has a dedicated time-domain survey that is expected to yield $\sim 10^6$ asteroseismic detections in the Galactic center (Huber et al. 2023; Weiss et al. 2025). For example, investigation of the dependence of the oscillation amplitude scaling relation on stellar activity in different evolutionary phases and wavelength (Sreenivas et al. 2025) will be important for the asteroseismic yield from upcoming missions.

ACKNOWLEDGMENTS

We are thankful to our anonymous referee for helpful comments that improved this manuscript. We thank Howard Isaacson for valuable input and comments on the paper. We gratefully acknowledge the tireless efforts of everyone involved with the *Kepler* mission. This work was supported by the National Aeronautics and Space Administration through the ADAP grant 80NSSC19K0597. M.S. is supported by the Research Corporation for Science Advancement through Scialog award No. 26080. M.S. also thanks the LSSTC Data Science Fellowship Program, which is funded

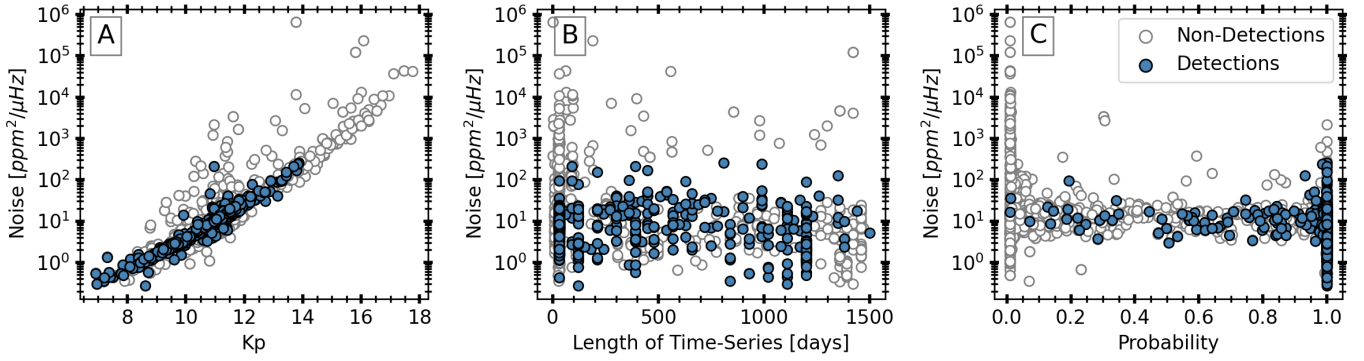


Figure 15. *Panel A:* Comparing distribution of white noise and *Kepler* apparent magnitude (*Kp*) between detections (blue points) and non-detections (unfilled). *Panel B:* same as Panel A, but investigating white noise as a function of length of time-series. *Panel C:* same as Panel A, but investigating white noise as a function of detection probability.

by LSSTC, NSF Cybertraining Grant No. 1829740, the Brinson Foundation, and the Moore Foundation; her participation in the program has benefited this work. D.H. acknowledges support from the Alfred P. Sloan Foundation and the Australian Research Council (FT200100871). This research made use of `lightkurve`, a Python package for *Kepler* and TESS data analysis.

Some of the data used in this paper were obtained at Keck Observatory, which is a private 501(c)3 non-profit organization operated as a scientific partnership among the California Institute of Technology, the University of California, and the National Aeronautics and Space Administration. The Observatory was made possible by the generous financial support of the W. M. Keck Foundation. The authors wish to recognize and acknowledge the very significant cultural role and reverence that the summit of Maunakea has always

had within the Native Hawaiian community. We are most fortunate to have the opportunity to conduct observations from this mountain.

Software: `astropy` (Astropy Collaboration et al. 2013, 2018), `lightkurve` (Lightkurve Collaboration et al. 2018), `Matplotlib` (Hunter 2007), `NumPy` (Harris et al. 2020), `Pandas` (Wes McKinney 2010), `pySYD` (Chontos et al. 2022), `SciPy` (Virtanen et al. 2020)

Facilities: Keck, *Kepler*

REFERENCES

- Aizenman, M., Smeyers, P., & Weigert, A. 1977, *A&A*, 58, 41
- Akeson, R., Armus, L., Bachelet, E., et al. 2019, arXiv e-prints, arXiv:1902.05569, doi: [10.48550/arXiv.1902.05569](https://doi.org/10.48550/arXiv.1902.05569)
- Angus, R., Aigrain, S., Foreman-Mackey, D., & McQuillan, A. 2015, *MNRAS*, 450, 1787, doi: [10.1093/mnras/stv423](https://doi.org/10.1093/mnras/stv423)
- Angus, R., Morton, T. D., Foreman-Mackey, D., et al. 2019, *AJ*, 158, 173, doi: [10.3847/1538-3881/ab3c53](https://doi.org/10.3847/1538-3881/ab3c53)
- Astropy Collaboration, Robitaille, T. P., Tollerud, E. J., et al. 2013, *A&A*, 558, A33, doi: [10.1051/0004-6361/201322068](https://doi.org/10.1051/0004-6361/201322068)
- Astropy Collaboration, Price-Whelan, A. M., Sipőcz, B. M., et al. 2018, *AJ*, 156, 123, doi: [10.3847/1538-3881/aabc4f](https://doi.org/10.3847/1538-3881/aabc4f)
- Baglin, A., Auvergne, M., Boissard, L., et al. 2006, in 36th COSPAR Scientific Assembly, Vol. 36, 3749
- Ballot, J., Barban, C., & van't Veer-Menneret, C. 2011, *A&A*, 531, A124, doi: [10.1051/0004-6361/201016230](https://doi.org/10.1051/0004-6361/201016230)
- Balona, L. A. 2020, *Frontiers in Astronomy and Space Sciences*, 7, 85, doi: [10.3389/fspas.2020.529025](https://doi.org/10.3389/fspas.2020.529025)
- Barnes, S. A. 2007, *ApJ*, 669, 1167, doi: [10.1086/519295](https://doi.org/10.1086/519295)
- Bastien, F. A., Stassun, K. G., Basri, G., & Pepper, J. 2013, *Nature*, 500, 427, doi: [10.1038/nature12419](https://doi.org/10.1038/nature12419)
- Batalha, N. M., Borucki, W. J., Bryson, S. T., et al. 2011, *ApJ*, 729, 27, doi: [10.1088/0004-637X/729/1/27](https://doi.org/10.1088/0004-637X/729/1/27)
- Beck, P. G., Montalbán, J., Kallinger, T., et al. 2012, *Nature*, 481, 55, doi: [10.1038/nature10612](https://doi.org/10.1038/nature10612)
- Bedding, T. R., Mosser, B., Huber, D., et al. 2011, *Nature*, 471, 608, doi: [10.1038/nature09935](https://doi.org/10.1038/nature09935)
- Berger, T. A., Huber, D., Gaidos, E., van Saders, J. L., & Weiss, L. M. 2020a, *AJ*, 160, 108, doi: [10.3847/1538-3881/aba18a](https://doi.org/10.3847/1538-3881/aba18a)

Table 3. Global asteroseismic values and errors measured with `pySYD` for 765 *Kepler* stars with detected solar-like oscillations. Oscillation amplitude at ν_{\max} , white noise, and height-to-background ratio are also provided. Previous values from other sources are provided for relevant targets. The source flag indicates the original source of asteroseismic measurements and the planet flag indicates whether the star is a planet host.

KIC ID	Source	Host	Literature				pySYD						
			ν_{\max}	$\sigma(\nu_{\max})$	$\Delta\nu$	$\sigma(\Delta\nu)$	ν_{\max}	$\sigma(\nu_{\max})$	$\Delta\nu$	$\sigma(\Delta\nu)$	A_{osc}	Noise	HBR
			[μHz]	[μHz]	[μHz]	[μHz]	[μHz]	[μHz]	[μHz]	[μHz]	[ppm ² / μHz]	[ppm ² / μHz]	
1430163	2	0	1867	92	84.60	2.00	1819	24	85.71	0.41	0.85	3.01	2.33
1435467	1	0	1382	19	70.56	0.09	1384	7	70.48	0.04	1.53	1.59	2.44
1725815	2	0	1045	47	55.40	1.30	1039	15	55.69	0.25	3.01	10.49	6.21
2010835	3	0	1312	19	72.73	4.52	1311	22	72.50	0.85	3.55	17.16	9.89
2162635	0	1					480	4	31.00	0.51	50.93	260.28	3.09
...

NOTE—The planet flag is 1 if the star is a planet host, and 0 otherwise. The source for literature global asteroseismic values refer to the following catalogs – 0: new detection, this work; 1: [Serenelli et al. \(2017\)](#); 2: [Chaplin et al. \(2014\)](#); 3: [Mathur et al. \(2022\)](#); 4: [Balona \(2020\)](#); 5: [Huber et al. \(2013\)](#); 6: [Lundkvist et al. \(2016\)](#); 7: [Li et al. \(2020a\)](#); 8: [Pinsonneault et al. \(2018\)](#); 9: [Lund et al. \(2017\)](#); 10: [Mosser et al. \(2014\)](#); 11: [White et al. \(2012\)](#); 12: [Chontos et al. \(2019\)](#); 13: [Bhalotia et al. \(2024\)](#). The full table in machine-readable format can be found online.

Table 4. Stellar properties of 765 solar-like oscillators in our sample, including T_{eff} from [Berger et al. \(2020b\)](#), RUWE from *Gaia* DR3, metallicity, and rotation periods. Stellar mass and radius were derived with scaling relations (Equations 6 & 7) using `pySYD` measurements.

KIC ID	Kp	T_{eff}	$\sigma(T_{\text{eff}})$	Radius	$\sigma(R)$	Mass	$\sigma(M)$	RUWE	[Fe/H]	Source([Fe/H])	Period	$\sigma(\text{Period})$	Source(P)
	[mag]	[K]	[K]	[R_{\odot}]	[R_{\odot}]	[M_{\odot}]	[M_{\odot}]		[dex]	[dex]	[days]	[days]	–
1430163	9.58	6609	141	1.56	0.02	1.54	0.05	0.92	−0.05	2	4.41	0.79	1
1435467	8.88	6391	128	1.73	0.01	1.41	0.03	5.73	−0.03	1	6.59	0.66	1
1725815	10.83	6212	120	2.05	0.02	1.47	0.05	4.04	−0.07	2	23.05	1.22	1
2010835	11.33	5927	117	1.49	0.03	0.96	0.07	0.97					
2162635	13.86	4952	118	2.73	0.04	1.07	0.08	1.01					
...

NOTE—The source flag for [Fe/H] refers to the following three catalogs – 1: [Serenelli et al. \(2017\)](#); 2: [Buchhave & Latham \(2015\)](#); 3: [Bruntt et al. \(2012\)](#). The source flag for rotation period refers to the following three catalogs – 1: [Santos et al. \(2021\)](#); 2: [McQuillan et al. \(2014\)](#); 3: [García et al. \(2014\)](#). The full table in machine-readable format can be found online.

Berger, T. A., Huber, D., van Saders, J. L., et al. 2020b, *AJ*, 159, 280, doi: [10.3847/1538-3881/159/6/280](#)

Bhalotia, V., Huber, D., van Saders, J. L., et al. 2024, *ApJ*, 970, 166, doi: [10.3847/1538-4357/ad4eb1](#)

Bonanno, A., Corsaro, E., Del Sordo, F., et al. 2019, *A&A*, 628, A106, doi: [10.1051/0004-6361/201935834](#)

Bonanno, A., Corsaro, E., & Karoff, C. 2014, *A&A*, 571, A35, doi: [10.1051/0004-6361/201424632](#)

Boro Saikia, S., Marvin, C. J., Jeffers, S. V., et al. 2018, *A&A*, 616, A108, doi: [10.1051/0004-6361/201629518](#)

Borucki, W. J., Koch, D., Basri, G., et al. 2010, *Science*, 327, 977, doi: [10.1126/science.1185402](#)

Boyajian, T. S., von Braun, K., van Belle, G., et al. 2013, *ApJ*, 771, 40, doi: [10.1088/0004-637X/771/1/40](#)

Brown, T. M., Gilliland, R. L., Noyes, R. W., & Ramsey, L. W. 1991, *ApJ*, 368, 599, doi: [10.1086/169725](#)

Bruntt, H., Basu, S., Smalley, B., et al. 2012, *MNRAS*, 423, 122, doi: [10.1111/j.1365-2966.2012.20686.x](#)

Buchhave, L. A., & Latham, D. W. 2015, *ApJ*, 808, 187, doi: [10.1088/0004-637X/808/2/187](#)

Campante, T. L., Chaplin, W. J., Lund, M. N., et al. 2014, *ApJ*, 783, 123, doi: [10.1088/0004-637X/783/2/123](#)

Cantiello, M., Fuller, J., & Bildsten, L. 2016, *ApJ*, 824, 14, doi: [10.3847/0004-637X/824/1/14](#)

Carter, J. A., Agol, E., Chaplin, W. J., et al. 2012, *Science*, 337, 556, doi: [10.1126/science.1223269](#)

Chaplin, W. J., Elsworth, Y., Isaak, G. R., Miller, B. A., & New, R. 2000, *MNRAS*, 313, 32, doi: [10.1046/j.1365-8711.2000.03176.x](#)

Chaplin, W. J., & Miglio, A. 2013, *ARA&A*, 51, 353, doi: [10.1146/annurev-astro-082812-140938](#)

Chaplin, W. J., Bedding, T. R., Bonanno, A., et al. 2011a, *ApJL*, 732, L5, doi: [10.1088/2041-8205/732/1/L5](#)

Table 5. KIC IDs and seismic measurements for the 22 stars which we did not confirm as detections. The source indicates the original paper that includes the target.

KIC	Source	$\Delta\nu$ [μHz]	$\sigma(\Delta\nu)$ [μHz]	ν_{max} [μHz]	$\sigma(\nu_{\text{max}})$ [μHz]
3730801	1	74.5	2.0		
11075448	1	78.1	2.9		
7418476	3	64.8	1.9	1359	29
9109988	3	96.5	2.7	1876	11
10969935	3	29.5	2.7	462	8
6048403	4	53.6	0.1	1039.9	2.0
7833587	4	64.9	0.2	1302.9	3.0
10593626	5	137.50	1.40		
6032981	5			35.1	0.6
4815520	6	136.0	0.3		
5383248	6	149.4	0.5		
6678383	6	56.5	0.4		
7887791	6	156.1	0.6		
7941200	6	130.1	0.5		
8753657	6	121.0	0.4		
9072639	6	85.2	0.3		
9579641	6	131.2	0.3		
10026544	6	26.0	0.6		
10130039	6	143.5	0.4		
10748390	6	186.6	0.4		
11600889	6	131.8	0.5		
11623629	6	161.1	0.4		

NOTE—Source key – 1: [Serenelli et al. \(2017\)](#); 3: [Mathur et al. \(2022\)](#); 4: [Balona \(2020\)](#); 5: [Huber et al. \(2013\)](#); 6: [Lundkvist et al. \(2016\)](#).

—. 2011b, *ApJL*, 732, L5, doi: [10.1088/2041-8205/732/1/L5](#)

Chaplin, W. J., Kjeldsen, H., Christensen-Dalsgaard, J., et al. 2011c, *Science*, 332, 213, doi: [10.1126/science.1201827](#)

Chaplin, W. J., Basu, S., Huber, D., et al. 2014, *ApJS*, 210, 1, doi: [10.1088/0067-0049/210/1/1](#)

Chen, H., & Rogers, L. A. 2016, *ApJ*, 831, 180, doi: [10.3847/0004-637X/831/2/180](#)

Chontos, A., Huber, D., Sayeed, M., & Yamsiri, P. 2022, *The Journal of Open Source Software*, 7, 3331, doi: [10.21105/joss.03331](#)

Chontos, A., Huber, D., Latham, D. W., et al. 2019, *AJ*, 157, 192, doi: [10.3847/1538-3881/ab0e8e](#)

Chontos, A., Huber, D., Berger, T. A., et al. 2021, *ApJ*, 922, 229, doi: [10.3847/1538-4357/ac1269](#)

Coelho, P., Barbuy, B., Meléndez, J., Schiavon, R. P., & Castilho, B. V. 2005, *A&A*, 443, 735, doi: [10.1051/0004-6361:20053511](#)

Corsaro, E., Bonanno, A., Kayhan, C., et al. 2024, *A&A*, 683, A161, doi: [10.1051/0004-6361/202348403](#)

Creevey, O. L., Doğan, G., Frasca, A., et al. 2012, *A&A*, 537, A111, doi: [10.1051/0004-6361/201117037](#)

Creevey, O. L., Metcalfe, T. S., Schultheis, M., et al. 2017, *A&A*, 601, A67, doi: [10.1051/0004-6361/201629496](#)

Dall, T. H., Bruntt, H., Stello, D., & Strassmeier, K. G. 2010, *A&A*, 514, A25, doi: [10.1051/0004-6361/200913710](#)

Doğan, G., Metcalfe, T. S., Deheuvels, S., et al. 2013, *ApJ*, 763, 49, doi: [10.1088/0004-637X/763/1/49](#)

Dziembowski, W. A., Gough, D. O., Houdek, G., & Sienkiewicz, R. 2001, *MNRAS*, 328, 601, doi: [10.1046/j.1365-8711.2001.04894.x](#)

Egeland, R., Soon, W., Baliunas, S., et al. 2017, *ApJ*, 835, 25, doi: [10.3847/1538-4357/835/1/25](#)

Evans, D. W., Riello, M., De Angeli, F., et al. 2018, *A&A*, 616, A4, doi: [10.1051/0004-6361/201832756](#)

Fröhlich, C., Andersen, B. N., Appourchaux, T., et al. 1997, *SoPh*, 170, 1, doi: [10.1023/A:1004969622753](#)

Fuller, J., Cantiello, M., Stello, D., Garcia, R. A., & Bildsten, L. 2015, *Science*, 350, 423, doi: [10.1126/science.aac6933](#)

Fulton, B. J., Petigura, E. A., Howard, A. W., et al. 2017, *AJ*, 154, 109, doi: [10.3847/1538-3881/aa80eb](#)

Furlan, E., Ciardi, D. R., Cochran, W. D., et al. 2018, *ApJ*, 861, 149, doi: [10.3847/1538-4357/aaca34](#)

Gaia Collaboration, Brown, A. G. A., Vallenari, A., et al. 2018, *A&A*, 616, A1, doi: [10.1051/0004-6361/201833051](#)

Gaia Collaboration, Vallenari, A., Brown, A. G. A., et al. 2023, *A&A*, 674, A1, doi: [10.1051/0004-6361/202243940](#)

García, R. A., Mathur, S., Salabert, D., et al. 2010, *Science*, 329, 1032, doi: [10.1126/science.1191064](#)

García, R. A., Ceillier, T., Salabert, D., et al. 2014, *A&A*, 572, A34, doi: [10.1051/0004-6361/201423888](#)

Gaulme, P., Jackiewicz, J., Appourchaux, T., & Mosser, B. 2014, *ApJ*, 785, 5, doi: [10.1088/0004-637X/785/1/5](#)

Gaulme, P., McKeever, J., Rawls, M. L., et al. 2013, *ApJ*, 767, 82, doi: [10.1088/0004-637X/767/1/82](#)

Gehan, C., Gaulme, P., & Yu, J. 2022, *A&A*, 668, A116, doi: [10.1051/0004-6361/202245083](#)

Gehan, C., Godoy-Rivera, D., & Gaulme, P. 2024, *A&A*, 686, A93, doi: [10.1051/0004-6361/202349008](#)

Gilliland, R. L., Marcy, G. W., Rowe, J. F., et al. 2013, *ApJ*, 766, 40, doi: [10.1088/0004-637X/766/1/40](#)

Ginzburg, S., Schlichting, H. E., & Sari, R. 2016, *ApJ*, 825, 29, doi: [10.3847/0004-637X/825/1/29](#)

—. 2018, *MNRAS*, 476, 759, doi: [10.1093/mnras/sty290](#)

Gomes da Silva, J., Santos, N. C., Adibekyan, V., et al. 2021, *A&A*, 646, A77, doi: [10.1051/0004-6361/202039765](#)

Hall, J. C. 2008, *Living Reviews in Solar Physics*, 5, 2, doi: [10.12942/lrsp-2008-2](#)

Table 6. Spectroscopic stellar parameters for 127 stars with available spectra from HIRES. We include **Specmatch** T_{eff} , $[\text{Fe}/\text{H}]$, and $\log g$ with respective error bars. We also provide asteroseismic masses and radii calculated with both **Specmatch** T_{eff} and isochrone based T_{eff} .

KIC ID	S_{HK}	$B - V$	T_{eff} [K]	$\sigma(T_{\text{eff}})$ [K]	$[\text{Fe}/\text{H}]$ [dex]	$\sigma([\text{Fe}/\text{H}])$ [dex]	$\log g$ [dex]	$\sigma(\log g)$ [dex]	$\log(R'_{\text{HK}})$	$\sigma(\log(R'_{\text{HK}}))$	R_{spec} [R_{\odot}]	M_{spec} [M_{\odot}]	R_{iso} [R_{\odot}]	M_{iso} [M_{\odot}]
1435467	0.14	0.48	6378	100	0.13	0.06	4.26	0.10	-5.02	0.03	1.73	1.41	1.73	1.41
2852862	0.12	0.49	6252	100	-0.04	0.06	4.10	0.10	-5.23	0.04	2.11	1.48	2.13	1.53
3123191	0.10	0.48	6313	100	-0.06	0.06	4.40	0.10	-5.60	0.08	1.33	1.02	1.34	1.03
3424541	0.15	0.51	6267	100	0.24	0.06	3.87	0.10	-4.99	0.03	2.80	2.04	2.82	2.09
3656476	0.14	0.68	5710	100	0.31	0.06	4.12	0.10	-5.11	0.02	1.29	1.01	1.28	1.00
...

NOTE—The full table in machine-readable format is available online.

- Hall, O. J., Davies, G. R., van Saders, J., et al. 2021, *Nature Astronomy*, 5, 707, doi: [10.1038/s41550-021-01335-x](https://doi.org/10.1038/s41550-021-01335-x)
- Handberg, R., & Lund, M. N. 2014, *MNRAS*, 445, 2698, doi: [10.1093/mnras/stu1823](https://doi.org/10.1093/mnras/stu1823)
- Harris, C. R., Millman, K. J., van der Walt, S. J., et al. 2020, *Nature*, 585, 357, doi: [10.1038/s41586-020-2649-2](https://doi.org/10.1038/s41586-020-2649-2)
- Hartmann, L., Soderblom, D. R., Noyes, R. W., Burnham, N., & Vaughan, A. H. 1984, *ApJ*, 276, 254, doi: [10.1086/161609](https://doi.org/10.1086/161609)
- Harvey, J. 1985, in *ESA Special Publication*, Vol. 235, *Future Missions in Solar, Heliospheric & Space Plasma Physics*, ed. E. Rolfe & B. Battrick, 199
- Hastie, T., Tibshirani, R., & Friedman, J. 2001, *The Elements of Statistical Learning*, Springer Series in Statistics (New York, NY, USA: Springer New York Inc.)
- Hatt, E., Nielsen, M. B., Chaplin, W. J., et al. 2023, *A&A*, 669, A67, doi: [10.1051/0004-6361/202244579](https://doi.org/10.1051/0004-6361/202244579)
- Hekker, S., Kallinger, T., Baudin, F., et al. 2009, *A&A*, 506, 465, doi: [10.1051/0004-6361/200911858](https://doi.org/10.1051/0004-6361/200911858)
- Hekker, S., Gilliland, R. L., Elsworth, Y., et al. 2011a, *MNRAS*, 414, 2594, doi: [10.1111/j.1365-2966.2011.18574.x](https://doi.org/10.1111/j.1365-2966.2011.18574.x)
- Hekker, S., Basu, S., Stello, D., et al. 2011b, *A&A*, 530, A100, doi: [10.1051/0004-6361/201016303](https://doi.org/10.1051/0004-6361/201016303)
- Hidalgo, S. L., Pietrinferni, A., Cassisi, S., et al. 2018, *ApJ*, 856, 125, doi: [10.3847/1538-4357/aab158](https://doi.org/10.3847/1538-4357/aab158)
- Hon, M., Huber, D., Kuszewicz, J. S., et al. 2021, *ApJ*, 919, 131, doi: [10.3847/1538-4357/ac14b1](https://doi.org/10.3847/1538-4357/ac14b1)
- Hon, M., Huber, D., Li, Y., et al. 2024, *ApJ*, 975, 147, doi: [10.3847/1538-4357/ad76a9](https://doi.org/10.3847/1538-4357/ad76a9)
- Howell, S. B., Rowe, J. F., Bryson, S. T., et al. 2012, *ApJ*, 746, 123, doi: [10.1088/0004-637X/746/2/123](https://doi.org/10.1088/0004-637X/746/2/123)
- Huang, Y., Liu, X. W., Yuan, H. B., et al. 2015, *MNRAS*, 454, 2863, doi: [10.1093/mnras/stv1991](https://doi.org/10.1093/mnras/stv1991)
- Huber, D., Stello, D., Bedding, T. R., et al. 2009, *Communications in Asteroseismology*, 160, 74, <https://arxiv.org/abs/0910.2764>
- Huber, D., Bedding, T. R., Stello, D., et al. 2011, *ApJ*, 743, 143, doi: [10.1088/0004-637X/743/2/143](https://doi.org/10.1088/0004-637X/743/2/143)
- Huber, D., Chaplin, W. J., Christensen-Dalsgaard, J., et al. 2013, *ApJ*, 767, 127, doi: [10.1088/0004-637X/767/2/127](https://doi.org/10.1088/0004-637X/767/2/127)
- Huber, D., Silva Aguirre, V., Matthews, J. M., et al. 2014, *ApJS*, 211, 2, doi: [10.1088/0067-0049/211/1/2](https://doi.org/10.1088/0067-0049/211/1/2)
- Huber, D., White, T. R., Metcalfe, T. S., et al. 2022, *AJ*, 163, 79, doi: [10.3847/1538-3881/ac3000](https://doi.org/10.3847/1538-3881/ac3000)
- Huber, D., Pinsonneault, M., Beck, P., et al. 2023, *arXiv e-prints*, arXiv:2307.03237, doi: [10.48550/arXiv.2307.03237](https://doi.org/10.48550/arXiv.2307.03237)
- Hunter, J. D. 2007, *Computing in Science & Engineering*, 9, 90, doi: [10.1109/MCSE.2007.55](https://doi.org/10.1109/MCSE.2007.55)
- Isaacson, H., & Fischer, D. 2010, *ApJ*, 725, 875, doi: [10.1088/0004-637X/725/1/875](https://doi.org/10.1088/0004-637X/725/1/875)
- Isaacson, H., Kane, S. R., Carter, B., et al. 2024, *ApJ*, 961, 85, doi: [10.3847/1538-4357/ad077b](https://doi.org/10.3847/1538-4357/ad077b)
- Jin, S., Mordasini, C., Parmentier, V., et al. 2014, *ApJ*, 795, 65, doi: [10.1088/0004-637X/795/1/65](https://doi.org/10.1088/0004-637X/795/1/65)
- Johnson, J. A., Aller, K. M., Howard, A. W., & Crepp, J. R. 2010, *PASP*, 122, 905, doi: [10.1086/655775](https://doi.org/10.1086/655775)
- Kirk, B., Conroy, K., Prša, A., et al. 2016, *AJ*, 151, 68, doi: [10.3847/0004-6256/151/3/68](https://doi.org/10.3847/0004-6256/151/3/68)
- Kjeldsen, H., & Bedding, T. R. 1995, *A&A*, 293, 87, <https://arxiv.org/abs/astro-ph/9403015>
- Kjeldsen, H., Bedding, T. R., Arentoft, T., et al. 2008, *ApJ*, 682, 1370, doi: [10.1086/589142](https://doi.org/10.1086/589142)
- Koch, D. G., Borucki, W. J., Basri, G., et al. 2010, *ApJL*, 713, L79, doi: [10.1088/2041-8205/713/2/L79](https://doi.org/10.1088/2041-8205/713/2/L79)
- Komm, R. W., Howe, R., & Hill, F. 2000, *ApJ*, 531, 1094, doi: [10.1086/308518](https://doi.org/10.1086/308518)
- Lee, E. J., Karalis, A., & Thorngren, D. P. 2022, *ApJ*, 941, 186, doi: [10.3847/1538-4357/ac9c66](https://doi.org/10.3847/1538-4357/ac9c66)

- Li, T., Bedding, T. R., Christensen-Dalsgaard, J., et al. 2020a, *MNRAS*, 495, 3431, doi: [10.1093/mnras/staa1350](https://doi.org/10.1093/mnras/staa1350)
- Li, Y., Bedding, T. R., Li, T., et al. 2020b, *MNRAS*, 495, 2363, doi: [10.1093/mnras/staa1335](https://doi.org/10.1093/mnras/staa1335)
- Lightkurve Collaboration, Cardoso, J. V. d. M., Hedges, C., et al. 2018, Lightkurve: Kepler and TESS time series analysis in Python, Astrophysics Source Code Library. <http://ascl.net/1812.013>
- Lindgren, L., Hernández, J., Bombrun, A., et al. 2018, *A&A*, 616, A2, doi: [10.1051/0004-6361/201832727](https://doi.org/10.1051/0004-6361/201832727)
- Lopez, E. D., & Fortney, J. J. 2014, *ApJ*, 792, 1, doi: [10.1088/0004-637X/792/1/1](https://doi.org/10.1088/0004-637X/792/1/1)
- Lopez, E. D., & Rice, K. 2018, *MNRAS*, 479, 5303, doi: [10.1093/mnras/sty1707](https://doi.org/10.1093/mnras/sty1707)
- Lorenzo-Oliveira, D., Freitas, F. C., Meléndez, J., et al. 2018, *A&A*, 619, A73, doi: [10.1051/0004-6361/201629294](https://doi.org/10.1051/0004-6361/201629294)
- Lund, M. N. 2019, *MNRAS*, 489, 1072, doi: [10.1093/mnras/stz2010](https://doi.org/10.1093/mnras/stz2010)
- Lund, M. N., Silva Aguirre, V., Davies, G. R., et al. 2017, *ApJ*, 835, 172, doi: [10.3847/1538-4357/835/2/172](https://doi.org/10.3847/1538-4357/835/2/172)
- Lundkvist, M. S., Kjeldsen, H., Albrecht, S., et al. 2016, *Nature Communications*, 7, 11201, doi: [10.1038/ncomms11201](https://doi.org/10.1038/ncomms11201)
- Mamajek, E. E., & Hillenbrand, L. A. 2008, *ApJ*, 687, 1264, doi: [10.1086/591785](https://doi.org/10.1086/591785)
- Marvin, C. J., Reiners, A., Anglada-Escudé, G., Jeffers, S. V., & Boro Saikia, S. 2023, *A&A*, 671, A162, doi: [10.1051/0004-6361/201937306](https://doi.org/10.1051/0004-6361/201937306)
- Mathur, S., García, R. A., Bugnet, L., et al. 2019, *Frontiers in Astronomy and Space Sciences*, 6, 46, doi: [10.3389/fspas.2019.00046](https://doi.org/10.3389/fspas.2019.00046)
- Mathur, S., García, R. A., Huber, D., et al. 2016, *ApJ*, 827, 50, doi: [10.3847/0004-637X/827/1/50](https://doi.org/10.3847/0004-637X/827/1/50)
- Mathur, S., Huber, D., Batalha, N. M., et al. 2017, *ApJS*, 229, 30, doi: [10.3847/1538-4365/229/2/30](https://doi.org/10.3847/1538-4365/229/2/30)
- Mathur, S., García, R. A., Breton, S., et al. 2022, *A&A*, 657, A31, doi: [10.1051/0004-6361/202141168](https://doi.org/10.1051/0004-6361/202141168)
- McQuillan, A., Mazeh, T., & Aigrain, S. 2014, *ApJS*, 211, 24, doi: [10.1088/0067-0049/211/2/24](https://doi.org/10.1088/0067-0049/211/2/24)
- Meibom, S., Barnes, S. A., Platais, I., et al. 2015, *Nature*, 517, 589, doi: [10.1038/nature14118](https://doi.org/10.1038/nature14118)
- Metcalf, T. S., Monteiro, M. J. P. F. G., Thompson, M. J., et al. 2010, *ApJ*, 723, 1583, doi: [10.1088/0004-637X/723/2/1583](https://doi.org/10.1088/0004-637X/723/2/1583)
- Metcalf, T. S., Chaplin, W. J., Appourchaux, T., et al. 2012, *ApJL*, 748, L10, doi: [10.1088/2041-8205/748/1/L10](https://doi.org/10.1088/2041-8205/748/1/L10)
- Metcalf, T. S., Creevey, O. L., Doğan, G., et al. 2014, *ApJS*, 214, 27, doi: [10.1088/0067-0049/214/2/27](https://doi.org/10.1088/0067-0049/214/2/27)
- Metcalf, T. S., Finley, A. J., Kochukhov, O., et al. 2022, *ApJL*, 933, L17, doi: [10.3847/2041-8213/ac794d](https://doi.org/10.3847/2041-8213/ac794d)
- Metcalf, T. S., Buzasi, D., Huber, D., et al. 2023, *AJ*, 166, 167, doi: [10.3847/1538-3881/acflf7](https://doi.org/10.3847/1538-3881/acflf7)
- Michel, E., Samadi, R., Baudin, F., et al. 2009, *A&A*, 495, 979, doi: [10.1051/0004-6361/200810353](https://doi.org/10.1051/0004-6361/200810353)
- Middelkoop, F. 1982, *A&A*, 107, 31
- Mosser, B., Michel, E., Appourchaux, T., et al. 2009, *A&A*, 506, 33, doi: [10.1051/0004-6361/200911917](https://doi.org/10.1051/0004-6361/200911917)
- Mosser, B., Belkacem, K., Goupil, M. J., et al. 2010, *A&A*, 517, A22, doi: [10.1051/0004-6361/201014036](https://doi.org/10.1051/0004-6361/201014036)
- Mosser, B., Elsworth, Y., Hekker, S., et al. 2012, *A&A*, 537, A30, doi: [10.1051/0004-6361/20111735210.1086/141952](https://doi.org/10.1051/0004-6361/20111735210.1086/141952)
- Mosser, B., Benomar, O., Belkacem, K., et al. 2014, *A&A*, 572, L5, doi: [10.1051/0004-6361/201425039](https://doi.org/10.1051/0004-6361/201425039)
- Murphy, S. J., Hey, D., Van Reeth, T., & Bedding, T. R. 2019, *MNRAS*, 485, 2380, doi: [10.1093/mnras/stz590](https://doi.org/10.1093/mnras/stz590)
- NASA Exoplanet Archive. 2024, Kepler Objects of Interest DR25, Version: YYYY-MM-DD HH:MM, NExScI-Caltech/IPAC, doi: [10.26133/NEA5](https://doi.org/10.26133/NEA5)
- Noyes, R. W., Hartmann, L. W., Baliunas, S. L., Duncan, D. K., & Vaughan, A. H. 1984, *ApJ*, 279, 763, doi: [10.1086/161945](https://doi.org/10.1086/161945)
- Owen, J. E., & Wu, Y. 2013, *ApJ*, 775, 105, doi: [10.1088/0004-637X/775/2/105](https://doi.org/10.1088/0004-637X/775/2/105)
- . 2017, *ApJ*, 847, 29, doi: [10.3847/1538-4357/aa890a](https://doi.org/10.3847/1538-4357/aa890a)
- Petigura, E. A. 2015, PhD thesis, University of California, Berkeley
- . 2020, *AJ*, 160, 89, doi: [10.3847/1538-3881/ab9fff](https://doi.org/10.3847/1538-3881/ab9fff)
- Pinsonneault, M. H., Elsworth, Y. P., Tayar, J., et al. 2018, *ApJS*, 239, 32, doi: [10.3847/1538-4365/aaebfd](https://doi.org/10.3847/1538-4365/aaebfd)
- Priestley, M. 1981, *Spectral Analysis and Time Series, Probability and mathematical statistics : A series of monographs and textbooks No. v. 1* (Academic Press). <https://books.google.com/books?id=RVTYvwEACAAJ>
- Raftery, A. 1995, *Sociological Methodology*, 25, 111, doi: [10.2307/271063](https://doi.org/10.2307/271063)
- Rauer, H., Catala, C., Aerts, C., et al. 2014, *Experimental Astronomy*, 38, 249, doi: [10.1007/s10686-014-9383-4](https://doi.org/10.1007/s10686-014-9383-4)
- Rauer, H., Aerts, C., Cabrera, J., et al. 2024, arXiv e-prints, arXiv:2406.05447, doi: [10.48550/arXiv.2406.05447](https://doi.org/10.48550/arXiv.2406.05447)
- Ricker, G. R., Winn, J. N., Vanderspek, R., et al. 2014, in *Society of Photo-Optical Instrumentation Engineers (SPIE) Conference Series*, Vol. 9143, Space Telescopes and Instrumentation 2014: Optical, Infrared, and Millimeter Wave, ed. J. Oschmann, Jacobus M., M. Clampin, G. G. Fazio, & H. A. MacEwen, 914320, doi: [10.1117/12.2063489](https://doi.org/10.1117/12.2063489)
- Santos, A. R. G., Breton, S. N., Mathur, S., & García, R. A. 2021, *ApJS*, 255, 17, doi: [10.3847/1538-4365/ac033f](https://doi.org/10.3847/1538-4365/ac033f)
- Sayeed, M., Huber, D., Wheeler, A., & Ness, M. K. 2021, *AJ*, 161, 170, doi: [10.3847/1538-3881/abdf4c](https://doi.org/10.3847/1538-3881/abdf4c)

- Sekiguchi, M., & Fukugita, M. 2000, *AJ*, 120, 1072, doi: [10.1086/301490](https://doi.org/10.1086/301490)
- Serenelli, A., Johnson, J., Huber, D., et al. 2017, *ApJS*, 233, 23, doi: [10.3847/1538-4365/aa97df](https://doi.org/10.3847/1538-4365/aa97df)
- Silva Aguirre, V., Basu, S., Brandão, I. M., et al. 2013, *ApJ*, 769, 141, doi: [10.1088/0004-637X/769/2/141](https://doi.org/10.1088/0004-637X/769/2/141)
- Silva Aguirre, V., Davies, G. R., Basu, S., et al. 2015, *MNRAS*, 452, 2127, doi: [10.1093/mnras/stv1388](https://doi.org/10.1093/mnras/stv1388)
- Silva Aguirre, V., Lund, M. N., Antia, H. M., et al. 2017, *ApJ*, 835, 173, doi: [10.3847/1538-4357/835/2/173](https://doi.org/10.3847/1538-4357/835/2/173)
- Skumanich, A. 1972, *ApJ*, 171, 565, doi: [10.1086/151310](https://doi.org/10.1086/151310)
- Soderblom, D. R. 2010, *ARA&A*, 48, 581, doi: [10.1146/annurev-astro-081309-130806](https://doi.org/10.1146/annurev-astro-081309-130806)
- Spada, F., & Lanzafame, A. C. 2020, *A&A*, 636, A76, doi: [10.1051/0004-6361/201936384](https://doi.org/10.1051/0004-6361/201936384)
- Spergel, D., Gehrels, N., Baltay, C., et al. 2015, arXiv e-prints, arXiv:1503.03757, doi: [10.48550/arXiv.1503.03757](https://doi.org/10.48550/arXiv.1503.03757)
- Sreenivas, K. R., Bedding, T. R., Huber, D., et al. 2025, *MNRAS*, 537, 3265, doi: [10.1093/mnras/staf220](https://doi.org/10.1093/mnras/staf220)
- Stassun, K. G., Kratter, K. M., Scholz, A., & Dupuy, T. J. 2012, *ApJ*, 756, 47, doi: [10.1088/0004-637X/756/1/47](https://doi.org/10.1088/0004-637X/756/1/47)
- Stello, D., Cantiello, M., Fuller, J., et al. 2016, *Nature*, 529, 364, doi: [10.1038/nature16171](https://doi.org/10.1038/nature16171)
- Stello, D., Chaplin, W. J., Basu, S., Elsworth, Y., & Bedding, T. R. 2009, *MNRAS*, 400, L80, doi: [10.1111/j.1745-3933.2009.00767.x](https://doi.org/10.1111/j.1745-3933.2009.00767.x)
- Stello, D., Huber, D., Bedding, T. R., et al. 2013, *ApJL*, 765, L41, doi: [10.1088/2041-8205/765/2/L41](https://doi.org/10.1088/2041-8205/765/2/L41)
- Thompson, S. E., Caldwell, D. A., Jenkins, J. M., et al. 2016, Kepler Data Release 25 Notes, Kepler Science Document KSCI-19065-002, id.3. Edited by Jon Jenkins and Michael R. Haas
- Ulrich, R. K. 1986, *ApJL*, 306, L37, doi: [10.1086/184700](https://doi.org/10.1086/184700)
- Van Eylen, V., Agentoft, C., Lundkvist, M. S., et al. 2018, *MNRAS*, 479, 4786, doi: [10.1093/mnras/sty1783](https://doi.org/10.1093/mnras/sty1783)
- van Saders, J. L., Ceillier, T., Metcalfe, T. S., et al. 2016, *Nature*, 529, 181, doi: [10.1038/nature16168](https://doi.org/10.1038/nature16168)
- Virtanen, P., Gommers, R., Oliphant, T. E., et al. 2020, *Nature Methods*, 17, 261, doi: [10.1038/s41592-019-0686-2](https://doi.org/10.1038/s41592-019-0686-2)
- Weiss, T. J., Downing, N. J., Pinsonneault, M. H., et al. 2025, arXiv e-prints, arXiv:2503.04999, doi: [10.48550/arXiv.2503.04999](https://doi.org/10.48550/arXiv.2503.04999)
- Wes McKinney. 2010, in Proceedings of the 9th Python in Science Conference, ed. Stéfan van der Walt & Jarrod Millman, 56 – 61, doi: [10.25080/Majora-92bf1922-00a](https://doi.org/10.25080/Majora-92bf1922-00a)
- White, T. R., Bedding, T. R., Gruberbauer, M., et al. 2012, *ApJL*, 751, L36, doi: [10.1088/2041-8205/751/2/L36](https://doi.org/10.1088/2041-8205/751/2/L36)
- Yu, J., Huber, D., Bedding, T. R., et al. 2018, *ApJS*, 236, 42, doi: [10.3847/1538-4365/aaaf74](https://doi.org/10.3847/1538-4365/aaaf74)
- . 2016, *MNRAS*, 463, 1297, doi: [10.1093/mnras/stw2074](https://doi.org/10.1093/mnras/stw2074)
- Zhou, J., Bi, S., Yu, J., et al. 2024, *ApJS*, 271, 17, doi: [10.3847/1538-4365/ad18db](https://doi.org/10.3847/1538-4365/ad18db)
- Zinn, J. C., Pinsonneault, M. H., Huber, D., et al. 2019, *ApJ*, 885, 166, doi: [10.3847/1538-4357/ab44a9](https://doi.org/10.3847/1538-4357/ab44a9)

APPENDIX

Figures A1 and A2 show the power spectra of the 50 new detections centered on ν_{\max} . In Figure A3, we show the 22 stars that were previously classified as detections but we did not find solar-like oscillations in them.

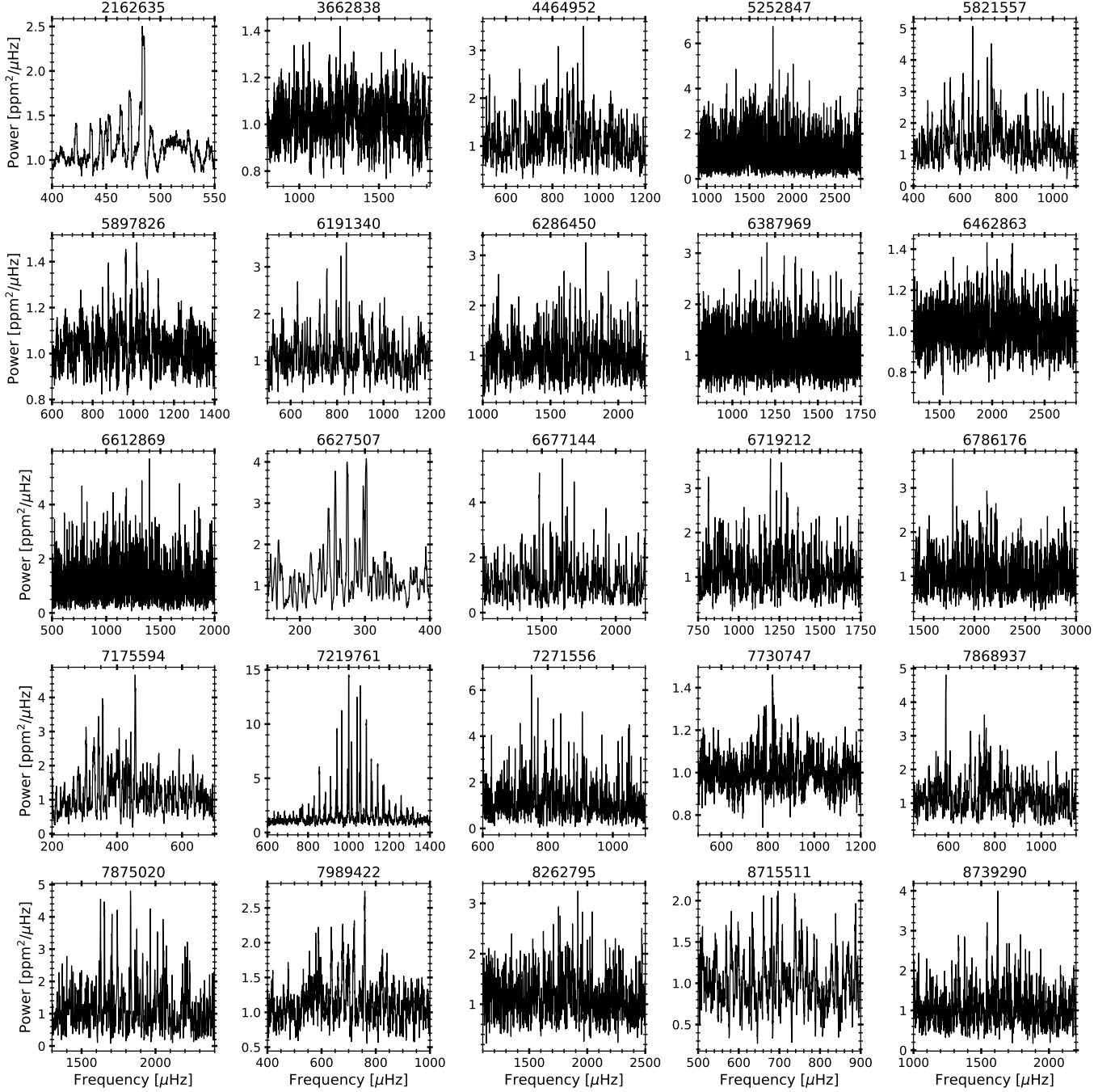


Figure A1. Smoothed and background corrected power spectra for 25 of the 50 new detections as found by pySYD, centered on ν_{\max} .

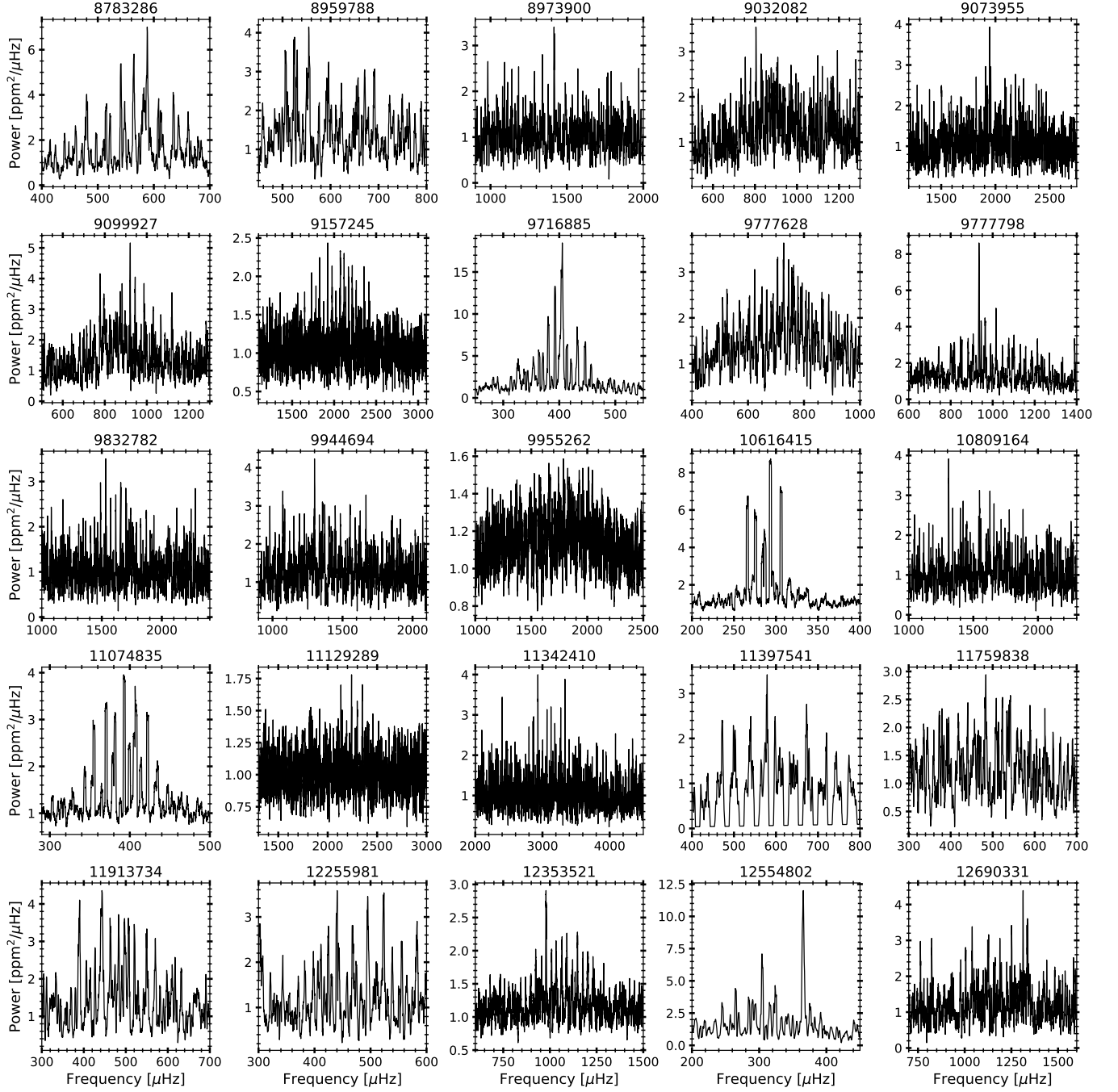


Figure A2. Same as Figure A1, for the other 25 of the 50 new detections found in this work.

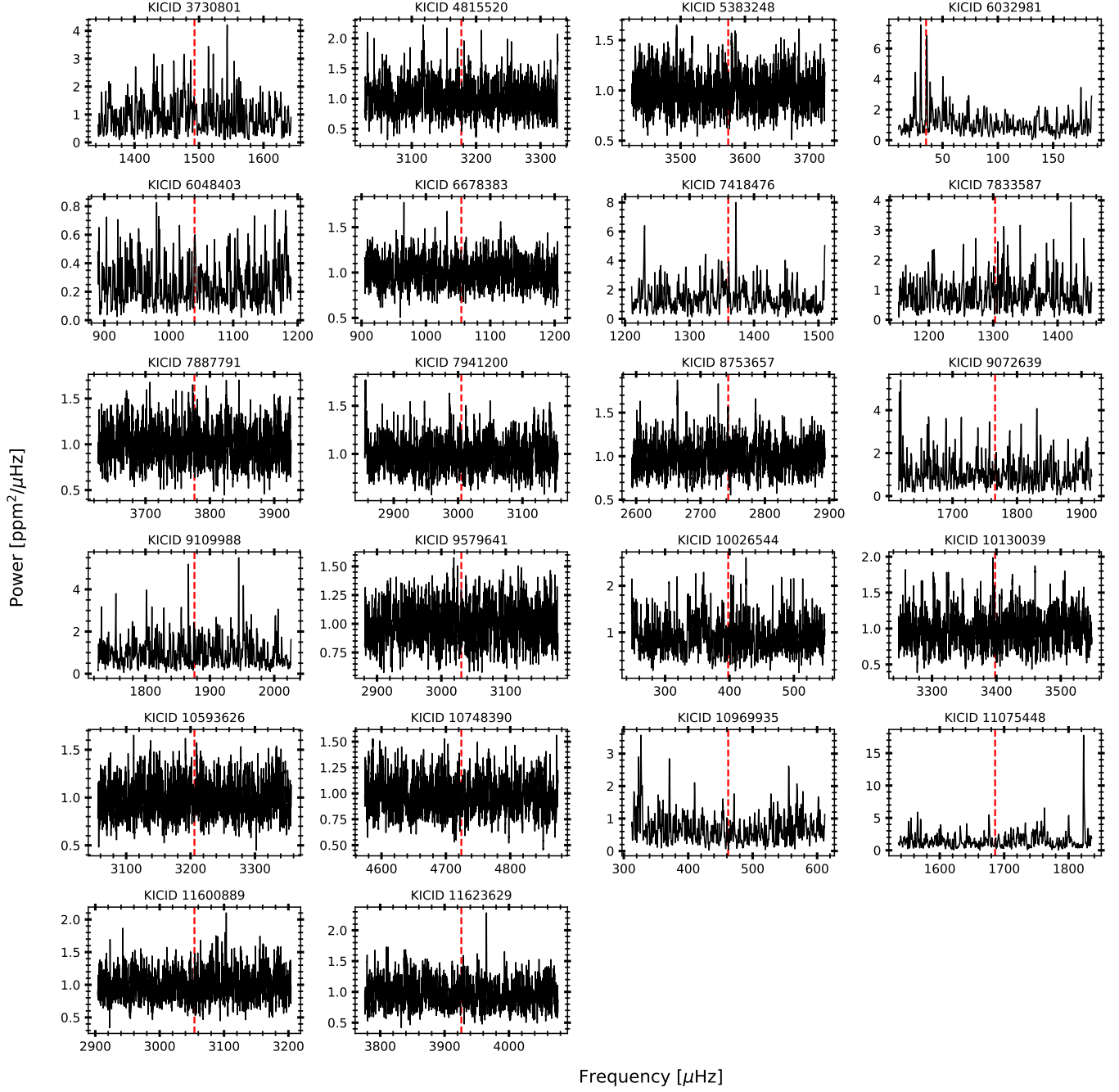


Figure A3. *Kepler* stars for which we did not find solar-like oscillations in DR25, but were previously classified as detections. Each subpanel shows the power spectrum of the target, centered on the expected ν_{max} as indicated by the red dashed line.